frontiers | Frontiers in Earth Science

TYPE Original Research
PUBLISHED 08 July 2024
DOI 10.3389/feart.2024.1405220

OPEN ACCESS

EDITED BY
Luis Gago-Duport,
University of Vigo, Spain

REVIEWED BY
Barbara Kremer,
Polish Academy of Sciences, Poland
Jamal El Kabouri,
University of Chouaib Doukali, Morocco

*CORRESPONDENCE
Fuencisla Cañadas,
fuencisla.canadas.16@ucl.ac.uk

†PRESENT ADDRESS
Fuencisla Cañadas,
Centre for Astrobiology (CAB), CSIC-INTA,
Madrid, Spain

RECEIVED 22 March 2024
ACCEPTED 29 May 2024
PUBLISHED 08 July 2024

CITATION
Cañadas F, Papineau D and She Z (2024),
Biotic and abiotic processes in Ediacaran
spheroid formation.
Front. Earth Sci. 12:1405220.
doi: 10.3389/feart.2024.1405220

Biotic and abiotic processes in Ediacaran spheroid formation

Fuencisla Cañadas[1*†], Dominic Papineau[1,2,3,4] and Zhenbing She[4,5]

[1]Department of Earth Sciences, University College London, London, United Kingdom, [2]London Centre for Nanotechnology, University College London, London, United Kingdom, [3]Centre for Planetary Sciences, University College London and Birkbeck College London, London, United Kingdom, [4]State Key Laboratory of Biogeology and Environmental Geology, China University of Geosciences, Wuhan, China, [5]School of Earth Sciences, China University of Geosciences, Wuhan, China

Organic-rich shales from the uppermost Doushantuo Fm. (South China) record one of the most negative carbonate carbon isotopic excursions in Earth's history, known as the Shuram excursion, and contain meter to micro-size spheroids. In this study, we use Raman and energy dispersive spectroscopy to identify and describe the most common diagenetic spheroids to refine our understanding of the profound perturbations of the carbon cycle and the evolution of pore fluid chemistry imprinted in the sedimentary Precambrian record, especially in the late Ediacaran. The presence of ^{13}C-depleted carbonate concretions or organic matter (OM) enclosed by lenticular dolomitic structures within the host shale unit suggests OM remineralisation and anaerobic oxidation, resulting in authigenic carbonate precipitation during the earliest stages of sediment diagenesis. Other mineralogical features, however, point to high levels of primary production, such as apatite bands that host spheroidal microfossils with highly fluorescent quartz and OM within abiotic concretions. These observations highlight the importance of considering co-occurring biotic and abiotic processes in explaining the formation of diagenetic spheroids in ancient sedimentary environments. From an astrobiology perspective, the interplay of biotic and abiotic processes reflects the complexity of early life systems and the environments that may exist on other terrestrial planets. Understanding the signatures of biotic and abiotic interactions in the Doushantuo Fm. is crucial for identifying potential biosignatures in extraterrestrial materials, thereby enhancing our understanding of life's universality and adaptability in diverse and extreme environments.

KEYWORDS

diagenetic spheroids, microfossils, early diagenesis, chemically oscillating reactions, abiotic oxidation

1 Introduction

Diagenetic spheroids are a group of sedimentological spheroidal to sub-ellipsoidal structures that include concretions, botryoids, granules and rosettes (Papineau et al., 2016; 2021; Dodd et al., 2018; Papineau, 2020). They may exhibit concentric layering and are typically composed of quartz, OM, dolomite, pyrite, ferric-ferrous oxides, and/or phosphates. Concretions generally present sizes >1 cm, granules between 1 cm and ~200 μm, and rosettes <~200 μm. Concretions are typically composed of authigenic aggregates of diagenetic minerals such as carbonate and quartz (Sellés-Martínez, 1996). They are common in organic-rich mudstones throughout the geological record. A significant

fraction of bicarbonate required for carbonate precipitation is thought to be supplied from the diagenetic decomposition of OM in the sediments. As such, concretions and other diagenetic spheroids provide insight into ancient biogeochemical processes and the evolution of pore fluid chemistry during the burial and before compaction of sediments (Raiswell and Fisher, 2000).

Member IV organic-rich shales within the Doushantuo Formation preserve a remarkable geological event known as the Shuram excursion, marked by one of the most significant negative carbonate carbon isotopic shifts in Earth's history. Interestingly, these organic-rich shales trace the subsequent return to pre-excursion values and, thus, to an equilibrium driven by high levels of primary production recorded in the C and N cycles (Cañadas et al., 2022). However, little is known about the sedimentary characteristics and organic-mineral associations at the microscopic scale, besides the hosted metre to centimetre size phosphatic and carbonate concretions (Jiang et al., 2011) as the most common sedimentological feature described up to date. Thus, new descriptions are required to refine our understanding of the profound perturbations that the carbon cycle imprinted in the Precambrian sedimentary record.

Carbonate and phosphatic concretions are widespread in the Doushantuo Fm. in South China (McFadden et al., 2008; Jiang et al., 2011; Zhu et al., 2013) and other Ediacaran successions worldwide (Gómez-Peral et al., 2014; Kitanaka et al., 2023) and have been attributed to both biogenic (Zhai et al., 2020; El Kabouri et al., 2023) and abiogenic (Papineau et al., 2021; El Kabouri et al., 2023) origin. Typically, carbonate concretions have been explained as biological processes such as microbial sulfate reduction or anaerobic oxidation of methane (Sellés-Martínez, 1996; Raiswell and Fisher, 2000; Dong et al., 2008). In contrast, phosphatic concretions are considered abiotic secondary mineral replacements after deposition (Kidder et al., 2003). While we agree in principle with this explanation for diagenesis, the process underlying the formation of key and recurring features remains without an explanation. In other words, none of these processes explains all the attributes of concretions, such as their characteristic spheroidal shapes, circularly concentric layers, radially aligned crystals, common association with fossils, or composed of specific kinds of mineral assemblages. Hence, it is essential to assess alternative abiotic processes that can explain both these patterns and the composition of their constituent minerals.

Abiotic chemically oscillating reactions (COR) represent a plausible mechanism that can explain the formation of diagenetic spheroids resulting from early diagenetic oxidation of biomass (Papineau et al., 2017; 2021; Papineau, 2020). One of these reactions, the Belousov-Zhabotinsky (BZ) reaction, involves the out-of-equilibrium oxidation of carboxylic acids (–COOH) like malonic acid ($CH_2(COOH)_2$) with strong halogen oxidants, such as bromate (BrO_3^-) and iodate (IO_3^-), and strong acids like sulfuric acid (H_2SO_4) to produce CO_2 (Zhabotinsky, 1991). This reaction produces characteristic concentric and radially geometric patterns, which have been used to suggest that this process occurs in nature (Ball, 2012). Specifically so far, COR have been proposed to explain the formation of rosettes in phosphorites (Papineau et al., 2016), granules in chert (Papineau et al., 2017; Dodd et al., 2018), and botryoids in malachite (Papineau, 2020), inside stromatolitic dolomite (Gabriel et al., 2021; Goodwin and Papineau, 2022), as well as in quartz botryoids from the Doushantuo cap carbonate (Papineau et al., 2021). Importantly, these studies document the common occurrence of OM within minerals of diagenetic spheroids such as carbonate and in association with apatite and sulphide.

This study uses optical microscopy, Raman spectroscopy and SEM observations to characterise organic-rich shales of Member IV of the Doushantuo Fm. from six stratigraphic sections that represent a comprehensive range of paleoenvironments. Through this combined methodology, we characterise the principal sedimentological and mineralogical features recorded in the sedimentary layers during one of the most intense perturbations in Earth's history, thereby contributing to our broader understanding of biosignatures and geological processes. In an astrobiological context, the study of diagenetic spheroids in the Ediacaran period has profound implications for our understanding of extraterrestrial life and planetary environments. If similar spheroidal structures were to be discovered on other terrestrial planets or moons, their analysis could offer invaluable clues about past biological and abiotic processes, potentially indicating the presence of ancient life or the conditions conducive to life.

2 Geology and sampling

The Ediacaran Doushantuo Fm. (635–551 Ma) was deposited on a passive continental margin along the south-eastern side of the Yangtze Block (red square Figure 1A). Paleoenvironmental reconstructions of the Yangtze platform have described three principal sedimentary facies distributed in a NE-SW orientation and formed by a carbonate platform, slope and basin facies (Jiang et al., 2011) (Figure 1B). In the Yangtze Gorges area (orange circle Figure 1B), the Doushantuo Fm. is subdivided into four lithostratigraphic members (Members I–IV), consisting of an alternation of dolostone, phosphorite and black shale. Member IV shales are situated in the uppermost part of the Doushantuo Formation (Figure 1C) and were deposited during a marine transgression. This member is regarded as a marker bed for stratigraphic correlation at the basin scale. From a sedimentological perspective, Member IV is relatively homogeneous across the basin, described as black and dark brown, well-sorted, and very fine-grained, with a massive organic-rich composition (TOC >10%) (Figure 2C) (Cañadas et al., 2022). It is thinly laminated to thin-bedded (Figure 1K), fissile, with rare grains, and contains pyrite (4%–12%) (McFadden et al., 2008). Additionally, it features oval carbonate and phosphatic concretions ranging in size from centimeters to meters, distributed throughout the member with no preferred distribution or orientation.

The stratigraphy of the Doushantuo Formation has remained a subject of continuous debate owing to its intricate nature, often proposing new interpretations. For instance, recent studies have highlighted a significant unconformity just preceding the onset of the Shuram excursion (Li et al., 2024). However, it is Member IV of the Doushantuo Fm. that attracts the most attention and discussion. Despite Member IV being considered a marker bed for stratigraphic correlation at the basin scale, its stratigraphic correlation in the proximal environment has been a matter of intense study. Several sections located in the western region of the Yangtze Gorges area (Figure 1B,

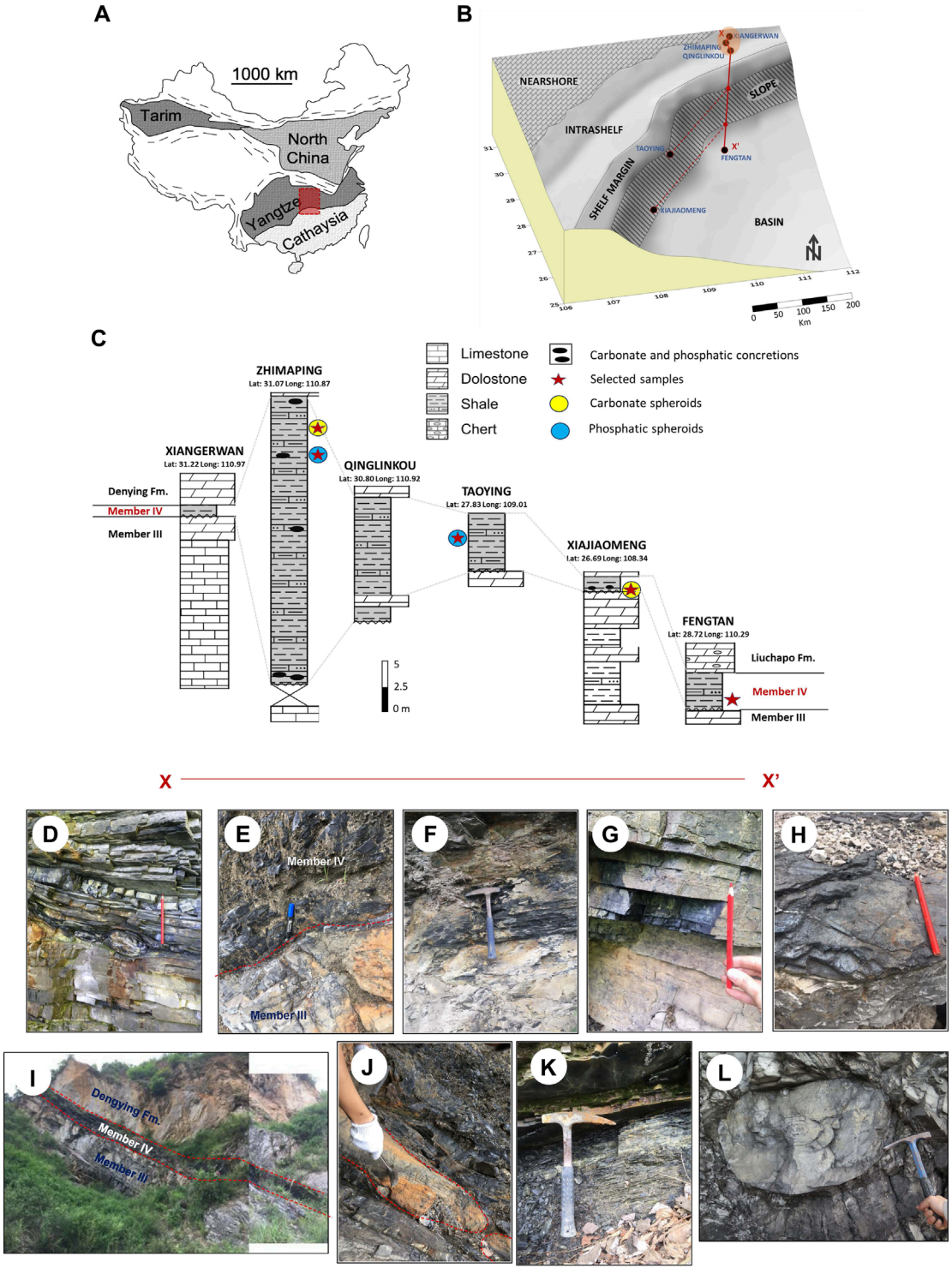

FIGURE 1
Maps, stratigraphic sections and outcrops images. **(A)** Map of China, with the Yangtze block in red. **(B)** Reconstructed Ediacaran depositional environments on the Yangtze block (modified from Jiang et al., 2011) with the platform-to-basin transect studied in red (X-X′). The orange circle marks the Yangtze Gorges area. **(C)** Stratigraphic sections studied. **(D)** Decimeter scale concretions at the base of Member IV in the Zhimaping section. **(E)** boundary between Member III and Member IV in the Qinglinkou section. **(F)** Organic-rich black shale in the Member IV of the Zhimaping section. **(G)** finely laminated black shale in the Member IV of the Taoying section. **(H)** Phosphorite bed in the Qinglinkou section. **(I)** Panoramic view of the Xiajiaomeng section showing the boundary among the different units. **(J)** Meter size concretion at the base of Member IV in the Xiajiaomeng section. **(K)** Black shale in the Member IV of the Fengtan section. **(L)** Meter size carbonate concretion from the Huangniuya section, located near the Qinglinkou section in the shelf lagoon area.

shelf lagoon) present two black shale layers separated by a dolostone interval, named upper black shale or Miaohe Member (MM), upper dolostone (UD) and lower black shale (LBS), respectively (Zhou et al., 2017). The presence of abundant macrofossils, known as the Miaohe biota in the MM, has been reported from the Miaohe section (Xiao et al., 2002) and more recently from Sanlihuang, Zhimaping and Maxi sections (Ye et al., 2019). It is uncertain how the MM, UD and LBS correlate with Member IV in the rest of the Yangtze Gorges area (central and eastern regions) and distal environments, where a single black shale layer of Member IV is present and may be partially chertified and similar to its overlying Liuchapo Formation (Jiang et al., 2011). This uncertainty has brought different stratigraphic interpretations whose principal difference lies in the age constraints of the Miaohe biota and, by extension, the duration and age of the Shuram Excursion in South China.

The first stratigraphic interpretation, known as the "A" correlation, proposes that the Miaohe Member is correlative with the overlying Shibantan Member (Dengying Fm.) (An et al., 2015) rather than Member IV of the Doushantuo Fm. The second stratigraphic interpretation, known as the "Z" correlation, proposes a conventional correlation in which the Miaohe Member, UD and LBS are equivalent to Member IV (Xiao et al., 2017; Zhou et al., 2017). In this case, the western region documents a complete lithostratigraphic sequence of the Upper Doushantuo Fm. The UD interval would be wedged and eventually disappear towards the central and eastern regions. This results in merging the upper and LBS in one interval. The third stratigraphic correlation considers the UD interval to be an allochthonous olistostrome due to large and small-scale slumping or faulting, in which case the two shale layers are from the same unit and equivalent to Member IV (Lu et al., 2013; Zhu et al., 2013). Whether any of the mentioned stratigraphic interpretations are correct is still a matter of debate, eventually influencing our understanding of the connection between the Shuram excursion and the Ediacaran-type biota. This study uses the correlation proposed in Cañadas et al. (2022), which used stratigraphic, paleontological, and geochemical arguments to support the "Z" correlation in the proximal area, whereby the black shales described in this study correlate with the Member IV of the Doushantuo Fm. and are interpreted to be equivalent to the Shuram excursion (Figure 2A).

The studied samples were collected from six different stratigraphic sections illustrated in Figure 1B: shelf lagoon (Xiangerwan, Zhimaping and Qinglinkou), upper slope (Taoying), lower slope (Xiajiaomeng) and basin (Fengtan). The sampling point in every stratigraphic section is marked in Figure 1C. The thickness of Member IV in these sections varies between 0.7 and 30 m. Metre-to-micrometre size carbonate concretions have been described in Zhimaping and Xiajiaomeng sections (Figures 1D–J). Centimetre-to-micrometre size phosphatic spheroids have been described in the Taoying and Zhimaping sections. Using Raman spectroscopy, Cañadas et al. (2022) estimated the maximum temperature reached for Member IV. They obtained a thermal basin distribution with temperatures between 280°C–289 °C in the proximal sections and between 300°C–311°C in the distal sections.

3 Methodology

3.1 Thin sections

Thin sections were made in the Department of Earth Sciences (UCL). First, raw samples (hand specimen) were trimmed using a diamond saw, ground and polished before cleaning with water, drying and mounting with epoxy onto standard 27 × 46 mm glass slides. Then, samples around 30 µm thickness were polished with progressively finer diamond-based compounds, down to the last step with 0.25 mm alumina, to produce polished thin sections suitable for optical microscopy. Finally, thin sections were scanned with a flatbed document scanner to create petrographic maps that could be annotated.

3.2 Optical microscopy

Petrographic descriptions of the sixteen selected thin sections were carried out in the Geological Spectroscopy Laboratory at the Department of Earth Sciences (UCL). The polarising microscope consists of an Olympus BX51 petrographic microscope with UIS2/UIS (Universal Infinity System) optical system. Imaging modes used were transmitted light, crossed polar, and reflected light. Objectives used for petrographic analysis were ×5, 10X, 20X, 50X, and 100X and no immersion oil was used. Petrographic descriptions in polished thin sections allowed the mapping of minerals and sedimentological targets onto the thin section maps to be subsequently analysed by micro-Raman spectroscopy.

3.3 Raman spectroscopy

Raman spectra and images were obtained in the Geological Spectroscopy Laboratory at UCL with a high-resolution WiTec alpha300 confocal Raman imaging system using a 532–nm wavelength laser with output laser power maintained at ~9 mW. This system used a grating with 600 lines per mm to provide a spectral resolution of around 4 cm^{-1} over a bandwidth of 4,000 cm^{-1}. Spectral accuracy was calibrated against an in-house gem-grade diamond standard and was better than 1 cm^{-1} over years of reproducibility tests. The acquisition time for each spectrum in Raman images was set between 0.5 and 0.8 s, and an optic fibre of 50 µm diameter was selected to provide confocality and acceptable signal intensity.

Data acquisition was made through the WITec Project Four Plus software. It allowed the creation of hyperspectral images for OM and specific minerals using peak intensity mapping for characteristic peaks in a scan in which each point of the scanned area is associated with a Raman spectrum. Raman hyperspectral scans were obtained at variable magnifications, mainly with ×50 and ×100 objectives, yielding variable spatial resolutions of up to 360 nm/pixel. All targets were analysed 1–5 µm below the thin section surface to minimise the detection of possible surface contaminants. In addition, polished thin sections were cleaned with an acetone rub using nitrile gloves and kimwipes to remove excess solvent, which helps to avoid potential surface contamination. Cosmic ray reduction was applied on all Raman spectra, and

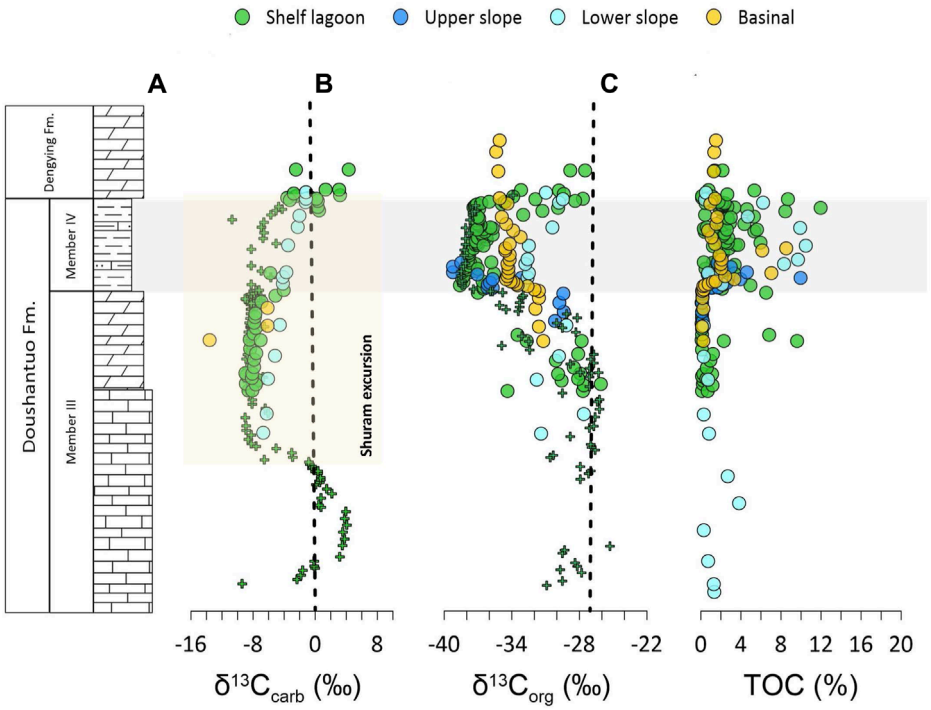

FIGURE 2
Chemostratigraphic columns of carbon isotope compositions in Doushantuo Member IV. **(A)** Carbonate carbon isotopes profiles for the different environments. The light-yellow square represents the stratigraphic interval that records the Shuram excursion. **(B)** Organic carbon isotopes. **(C)** Total organic carbon content. The grey area highlights the organic-rich shales of Member IV. Vertical dashed lines from left to right show Peedee belemnite and isotopic fractionation imparted to biomass by primary producers. Data in circles from Cañadas et al. (2022) and in crosses from McFadden et al. (2008).

their backgrounds were fitted to a polynomial function of order 7 and subtracted. Raman hyperspectral images were generated with the WITec Project Four Plus software by mapping the primary peak intensities diagnostic for specific mineral phases, including 465 cm^{-1} for quartz in blue, 1,090 cm^{-1} for dolomite in green, 965 cm^{-1} for apatite in turquoise, 515 cm^{-1} for feldspar, 990 cm^{-1} for barite, and 148 cm^{-1} for anatase. This approach produces micro-Raman images in which colours and spectra are correlated with optical properties to identify OM and associated minerals, which is ideal for understanding their petrographic distribution.

For OM, represented in red colour in hyperspectral images, the Raman spectrum is composed of two prominent peaks: the disordered (D) band (~1,350 cm^{-1}) and the graphite (G) band (~1,594 cm^{-1}), that represent represents sp^3-hybridised C atoms bonded to variable heteroatoms, and sp^2-hybridised C atoms bonded to three other atoms, respectively. When disordered, the OM Raman spectrum presents additional bands named D2 (~1,620 cm^{-1}), D3 (~1,510 cm^{-1}) and D4 (~1,245 cm^{-1}) bands (Beyssac et al., 2002). The bands mentioned above are calculated after deconvoluting the spectra range from 1,090 to 1700 cm^{-1} using Lorentzian functions. Additional key Raman spectral parameters that helped characterise the OM are the full width at half maximum (FWHM) of D and G bands and the I-1350/1,600 ratio. Figure 3 shows the peak-fitting and deconvolution of the Raman spectrum for Member IV.

3.4 Scanning electron microscopy

A Carl Zeiss EVO25 scanning electron microscope with an Oxford Instrument Xmax 80 electron dispersive spectrometer (EDS) detector was used at the Institute of Archaeology (UCL). Eight thin sections were selected for analysis and carbon-coated using a Quorum Technologies K975X carbon coater before analysis. Because of the necessary carbon coating, all EDS analyses were performed after micro-Raman examinations. The working distance was 8.5 mm, with an electron beam of 20 keV. Spectra were collected using Oxford Instruments Aztec 5.0 software, optimised against a pure cobalt standard before data collection, with a deadtime of approximately 40% on the cobalt. X-ray maps were collected with a pixel resolution of 1,024 * 768 pixels and a dwell time of 200 microseconds per pixel. Detection of distinctive x-ray emissions from the sample was done by energy dispersive spectroscopy (EDS) to detect elements and provide independent, quantitative confirmation of mineral compositions. ZAF correction was applied to minimise the impact of the atomic number, absorption, and fluorescence excitation effects.

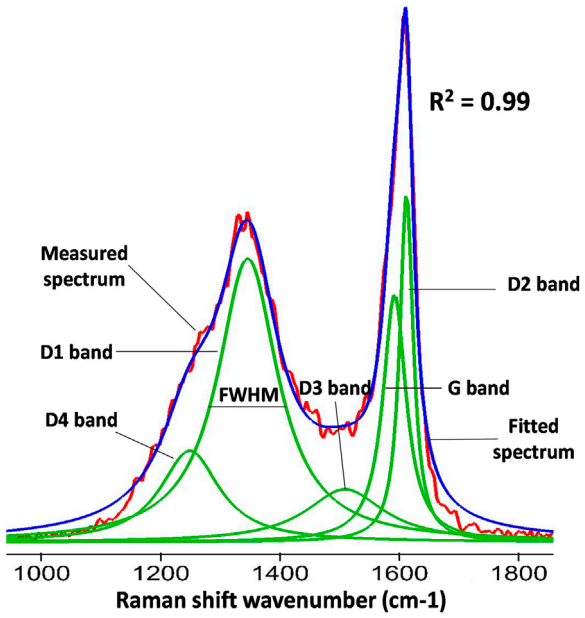

FIGURE 3
Lorentzian peak-fitting of the Raman spectrum for Member IV. The two first-order Raman bands of organic matter at ~1350 cm-1 and ~1600 cm-1 are represented. Peak decomposition in bands (G, D1, D2, D3 and D4) and the parameter FWHM (full width at half maximum) are shown. The coefficient of variation (R2) compares the original spectrum (red) with the fitted Raman spectrum (blue). Example from Cañadas et al. (2022) of the proximal environment (Qinglinkou section).

4 Results

4.1 Microscopic spheroidal objects

Diagenetic spheroids are found in the shelf lagoon and lower slope environment and are primarily formed of carbonate and phosphatic concretions (>1 cm) and rosettes (<200 µm) (Figures 1D, J, L, 4–7). Concretions present variable sizes and morphologies, between 10–20 cm and with an ellipsoidal shape (Figure 1D). Metre size concretions are also found in the area (Figure 1L). However, micrometre size spheroids are mostly dolomitic, with average diameters of 95 ± 35 µm (n=12) (Figure 4A), with spherical (Figure 5C) to ellipsoidal (Figures 5A, B, D, E, H) morphologies. Occasionally, dolomitic spheroids can reach diameters between 250–500 µm (Figures 5A, B, D, E). The core of rosettes observed in Member IV is circularly concentric with an inner core of OM surrounded by dolomite rims, formed by individual dolomite crystals between 5–20 µm (Figures 5B, C) that sometimes form aggregates (Figures 5D, E).

Although restricted to phosphatic concretions (Figure 6A), coccoidal morphologies resembling microfossils are also observed in Member IV. They present variable sizes between 5–20 µm with average diameters of 10.0 ± 3.0 µm (n=277) (Figures 4C, D) and are hosted in pale and dark bands and appear randomly and densely distributed. Raman and SEM results reveal that apatite is the primary component of the pale bands' matrix (Figures 6D–F, H). The coccoidal shapes preserve their original spheroidal shape with no identifiable internal structures. In general, these are isolated and not interconnected. The vast majority of these microfossil-like objects have been replaced by quartz (Figures 6C, D), whereas other coccoidal shapes show a partial quartz replacement with an inner core of OM surrounded by a quarzitic rim (red arrows in Figure 6G).

Additional diagenetic spheroids in Member IV occur in the upper slope environment in the form of microscopic sub-spheroidal morphologies (Figure 7). They have an average diameter of 59.0 ± 8.0 µm (n=6) and are surrounded by a quartz rim up to 15 µm wide (Figure 7B). The inner core is composed of highly fluorescent OM (HF-OM) and phosphate minerals (Figures 7B, C). In some of these spheres, barite crystals up to 25 µm long are found to replace the phosphatic phase (Figures 7B, C, E). In some cases, the spheroids have sizes up to 50 µm. They present characteristic concentric layers with distinctive mineral zonation alternating pale and dark grey from the core towards the outer rim (Figure 7G). SEM analyses show that the pale-grey layers correspond to the strengite phase based on its Fe and P content (Figures 7G, H, spectrum 1) and that the dark-grey layers correspond to the variscite phase based on its Al and P content (Figures 7G, H, spectrum 2).

4.2 Mineralogical and organic matter occurrence

Samples are primarily composed of clays, carbonates, phosphates and OM. In addition, accessory minerals such as barite, pyrite, feldspar and anatase are also present. Carbonate minerals are exclusively found in Zhimaping (proximal section) (Figure 5F–H) and in Xiajiaomeng (distal section) (Figures 5A–E). These carbonate minerals are generally present as euhedral to subhedral crystals and commonly form spheroids and ellipsoids. The carbonate phase is identified as dolomite from the Raman peaks at 157, 283, 714 and 1,090 cm^{-1} (Figure 5J). Note that the dolomite peaks in Zhimaping and Xiajiaomeng are slightly shifted compared to distinctive dolomite peaks (170, 290, 720 and 1,095 cm^{-1}). However, the EDS spectra shown in Figure 5I from carbonates in Figure 5G, with peaks for Ca, Mg, C, and O, support the occurrence of dolomite as the primary carbonate phase. Phosphate minerals in Member IV are only found in the shelf lagoon (Zhimaping) and the upper slope (Taoying). In the shelf lagoon, phosphates appear in horizontal apatite bands, up to 200 µm thick, that host variable amounts of black and white microfossil-like structures (Figure 6). Characteristic Raman peak at 965 cm^{-1} (Figure 6E) and EDS spectra with peaks for P, Ca and F (Figure 6H) reveal that the phosphate phase corresponds to fluorapatite. In the upper slope, however, phosphates appear to form microscopic spheroidal morphologies (Figures 7B, C, E, G). Raman spectra show these spheroidal morphologies are associated with highly fluorescent OM (HF-OM in Figure 7B) and surrounded by a rim of similarly sized quartz crystals and elongated barite grains (Figure 7B). However, complementary SEM analyses reveal the presence of strengite [$Fe^{3+}PO_4 \cdot 2H_2O$) and variscite [$Al^{3+}PO_4 \cdot 2H_2O$) associated with the highly fluorescent OM fraction (Figures 7G, H). The cryptocrystalline nature of these minerals in the spheroids is consistent with the high fluorescence and lack of peaks other than OM in Raman spectra.

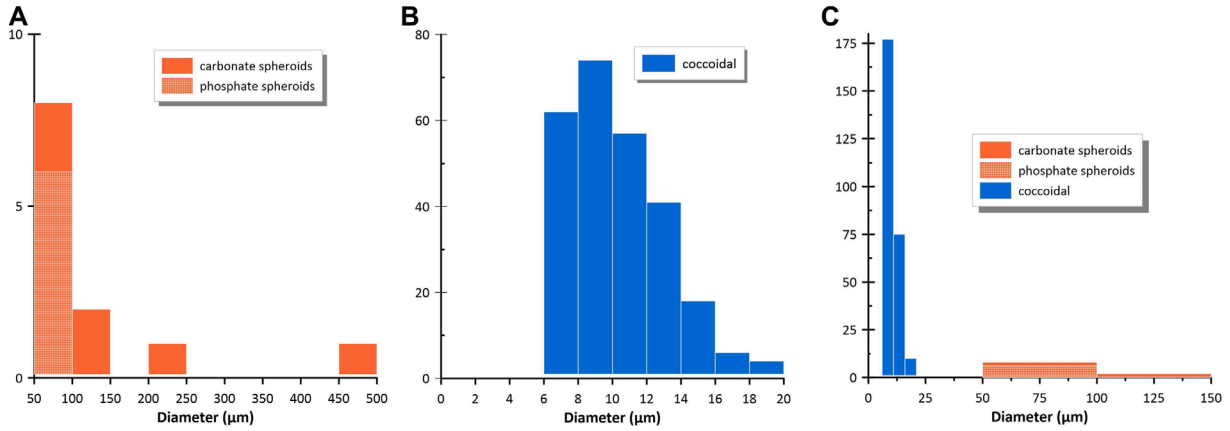

FIGURE 4
Histograms for the different spheroids in Member IV. **(A)** frequency for diagenetic carbonate (n=12; avg. 95 ± 35 µm) and phosphatic spheroids (n=6; avg. 59.0 ± 8.0). **(B)** Frequency for coccoidal (n=277; avg. 10.0 ± 3.0) spheroids in phosphatic-rich samples. **(C)** Relative frequency of the different spheroids found in Member IV for comparison.

Sulfur-bearing minerals in the studied samples predominantly occur in the form of barite [$BaSO_4$], jarosite [$KFe_3(SO_4)_2(OH)_6$] and pyrite [FeS_2]. Barite is identified in proximal and distal sections from its diagnostic Raman peaks at 455 and 989 cm^{-1} (Figures 7D, E). In the upper slope, barite is present as small and dispersed irregular crystals with sizes <10 µm, associated with quartz, filling voids and partially replacing organic-rich spheroidal morphologies (Figures 7B, C, E). In the basin section, barite appears as isolated euhedral crystals up to 50 µm embedded in an organic-rich matrix with no signs of grain dissolution (Figure 8B). Jarosite is exclusively found in the Fengtan section (distal environment). These crystals are subhedral brownish grains up to 40 µm in size without any preferential orientation (Figure 8B). This mineral is confirmed by Raman spectra, which show characteristic peaks at 221, 433, 625, 1,008 and 1,102 cm^{-1} (Figure 8E). Pyrite is also commonly found in all the studied samples, except those from Taoying. It is identified from its yellow reflective colour and characteristic Raman peaks at 345 and 381 cm^{-1} (Figure 5J). Pyrite mostly occurs as rounded, framboidal, subhedral, and euhedral habits with sizes between 10 µm and 2 mm.

Feldspars are also present in the studied samples. They exhibit variable sizes between 5–30 µm in the upper slope (Figure 7F) and 5–40 µm in the deep basin (Figure 8D). In these environments, feldspars are generally subangular or elongated in shape and with no preferred orientation. Characteristic Raman peaks confirm this mineral at 467 and 513 cm^{-1} (Figure 7D) correspond to either polymorph orthoclase or microcline [$KAlSi_3O_8$] based on elemental analyses with 11% K, 9% Al, 32% Si and 48% O of targeted minerals (Spectrum 3 Figure 8F).

Anatase (TiO_2) is present in all studied environments and shows characteristic Raman peaks at 146 (very strong), 398, 517 and 638 cm^{-1} (Figures 6E, 7D, 8E). However, anatase crystals have different size distributions related to specific mineral associations. For example, in samples associated with sulfur-bearing minerals (pyrite and/or jarosite), anatase is randomly distributed within the matrix and mainly occurs in the form of subhedral and elongated crystals <7.5 µm and most often <5 µm (Figure 8B). However, in samples where it is associated with apatite or barite, anatase has rounded and sub-rounded morphologies. It occurs as isolated crystals or forming aggregates between 5 and 15 µm (Figure 7F).

Organic matter presents the characteristic Raman D and G peaks at ~1,335 and 1,604 cm^{-1} (Figures 5J, 6H, 7D, 8E). Three different types of kerogen structures are identified in Member IV, as reported by Cañadas et al. (2022), who concluded that, after evaluating the potential impact of variable degradation and maturation, the different kerogens corresponded to variable dominance of organic carbon sources (photosynthetic vs. secondary). Kerogen "type-A" represents OM sourced from photosynthetic production and presents a wide D1 band, a more intense and narrower G band, and an I-1350/1,600 ratio of 0.6–0.7 (Table 1, Figures 5J, 6H). Kerogen "type-B" corresponds to OM resulting from secondary productivity and is characterised by narrower D1 and G bands and a resolvable shoulder of the D4 band at ~1,220 cm^{-1}, with an I-1350/1,600 ratio of 0.8 (Table 1, Figure 8E). And lastly, kerogen "type-C" represents mixed OM formed by primary and secondary production fractions, with combined features from type-A and B kerogens based on a more intense G band, like type-A, and narrower D1 and G bands, with an I-1350/1,600 ratio of 1 (Table 1 and Figure 7D). The three kerogen types are characterised by a specific distribution within the basin and a specific mineral association: 1) Kerogen "type-A" occurs in the shelf lagoon and lower slope and is primarily associated with dolomite, phosphates (apatite), anatase and pyrite; 2) Kerogen "type-B" is found in the basin and appears predominantly associated with Ba- and Fe-sulfates, anatase and large euhedral pyrite; and 3) Kerogen "type-C" occurs in the upper slope and is associated with phosphates (strengite-variscite), barite and alkali-bearing phases (feldspar). Table 1 present a detailed summary of the Raman parameters for OM, alongside the associated mineralogy and Table 2 presents characteristics of the diagenetic spheroid according to the mineral association identified in the organic-rich shales of Member IV.

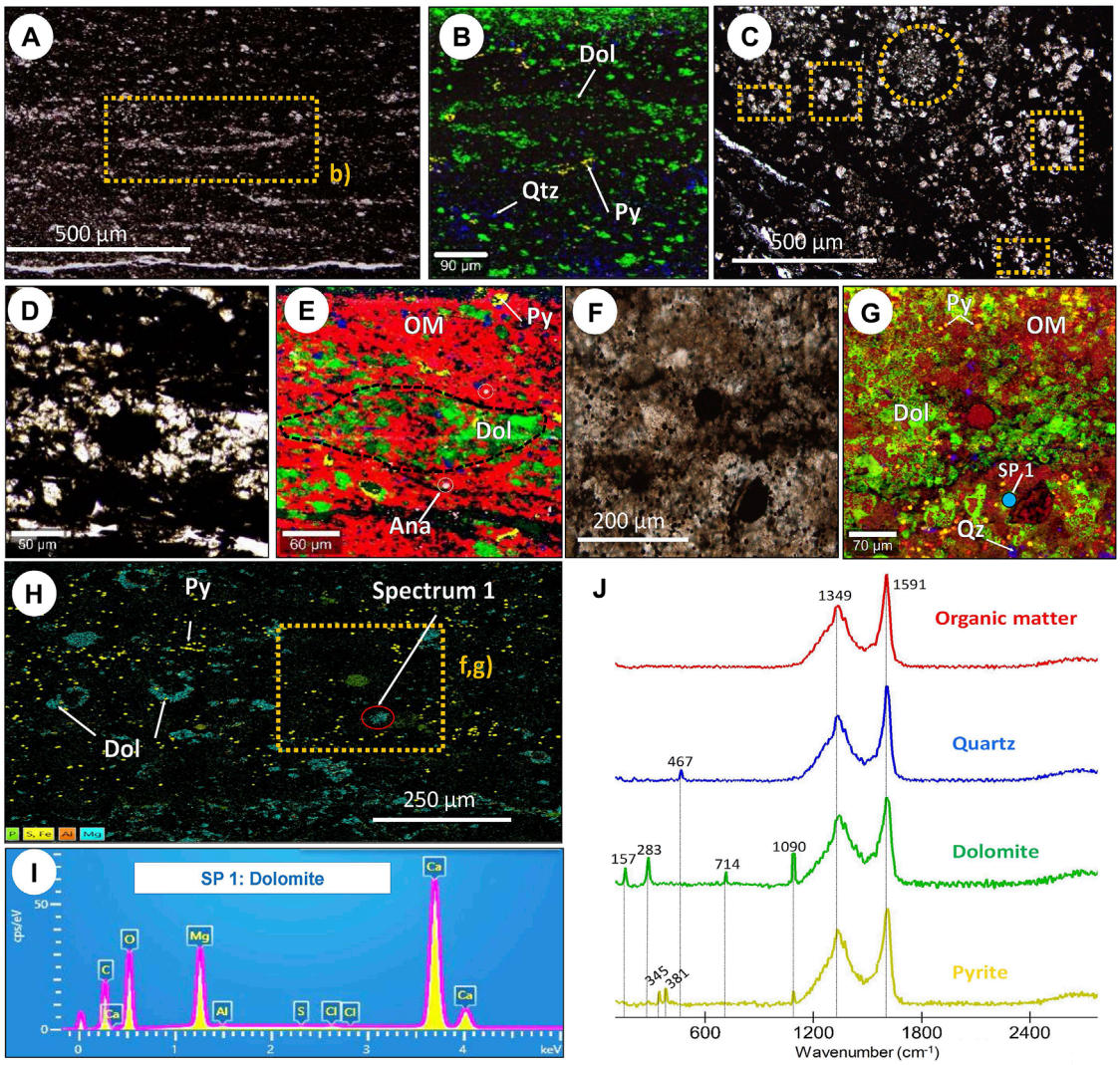

FIGURE 5
Petrographic, Raman and SEM characteristics of dolomitic diagenetic rosettes in the Zhimaping and Xiajiaomeng sections (shelf area and lower slope). **(A)** Thin section from the Xiajiaomeng section, located in the lower slope environment, showing massive and dark organic-rich shale with carbonate crystals and diagenetic rosettes. **(B)** Raman hyperspectral map of **(A)** representing the mineral fraction. The colours in the hyperspectral maps correspond to the colours in the Raman spectra. **(C)** Thin section from the Xiajiaomeng section showing different diagenetic structures. Orange squares indicate OM enclosed by spheroidal and ellipsoidal dolomitic rims, and orange circle shows dolomitic aggregates formed by individual dolomite crystals. **(D)** Dolomitic spheroid from the Xiajiaomeng section with a rim formed by individual rhombohedral crystals. **(E)** Raman hyperspectral image of d) indicating the distribution of OM and mineral fractions. The dotted black line shows the contour of the lense-shaped dolomitic spheroid. **(F)** Thin section from the Zhimaping section, located in the shelf lagoon environment. It is formed by organic-rich dolomitic shale with irregular laminations rich in OM **(G)** Raman spectra of the main minerals in **(F)** showing OM and associated minerals in the Zhimaping section. **(H)** EDS map of **(G)** showing the dolomitic rims in ellipsoidal morphologies and pyrite distribution associated with organic spheroidal morphologies. **(I)** EDS spectrum of dolomite. **(J)** Raman hyperspectral map of **(G)** representing the mineral fraction. The colours in the hyperspectral maps correspond to the colours in the Raman spectra. SP in **(G)** and **(I)** = spectrum.

5 Discussion

5.1 Carbonate spheroids

Carbonate diagenetic spheroids are widespread in organic-rich shales and are found in a large range of size and morphology, although usually spherical and ellipsoidal. Their origin is commonly explained as the result of different styles of abiotic physical growth. The two principal styles are replacement growth, where host sediments become incorporated into a concretionary body via extensive cementation of pore spaces, and displacive growth, which occurs when sedimentary beds are forced apart by the development of carbonate minerals (Sellés-Martínez, 1996). In Member IV, two principal types of carbonate diagenetic spheroids are documented. The first group, concretions, includes metre to centimetre size concretions, between 2 cm and 1 m, generally isolated, ellipsoidal and aligned with the sedimentary bedding (Figures 1D, L, J) (Dong et al., 2008; 2013; Zhou et al., 2017). In addition, this group presents characteristic displacive growth where host rock laminations are bent around the

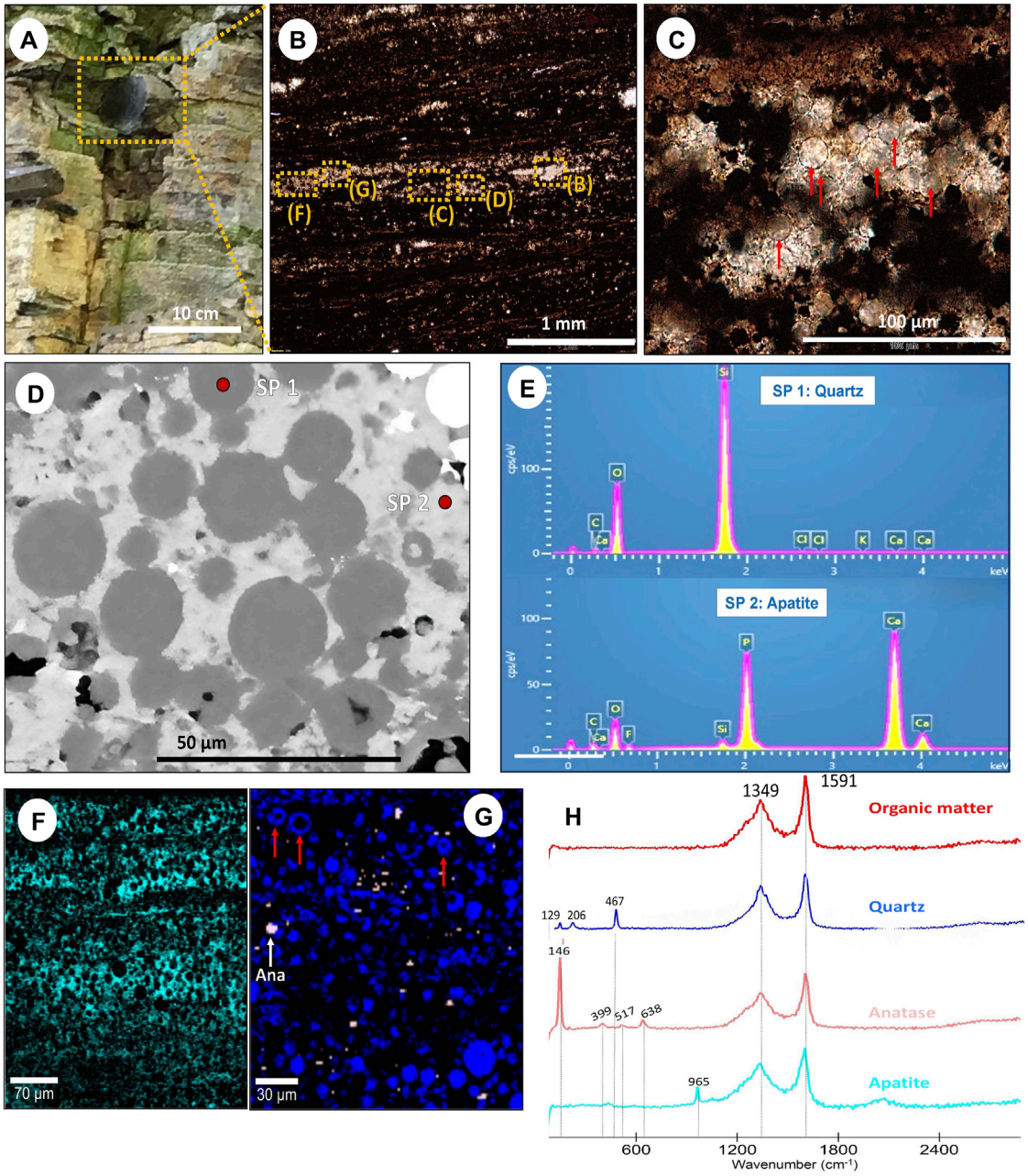

FIGURE 6
Petrographic, Raman and SEM characteristics of coccoidal microfossils in phosphatic concretions in the Zhimaping section (shelf area). **(A)** Phosphatic concretion at the top of Member IV (yellow dashed box) from the Zhimaping section (shelf lagoon). **(B)** Thin section composed of organic-rich shale with alternating pale brown and black bands **(C)** Plane polarized light image. Red arrows highlight ghostly coccoidal microfossils. **(D)** Backscattered electron image of **(B)**. **(E)** EDS spectra of quartz replacing the coccoidal microfossils and apatite in the matrix. **(F)** Raman hyperspectral image showing the apatite bands in which the coccoidal microfossils occur. **(G)** Raman hyperspectral image of coccoidal microfossils either totally or partially replaced by quartz (red arrows). The colours in the hyperspectral image correspond to the colours in the Raman spectra. **(H)** Raman spectra of **(B)** showing OM and associated minerals. SP in **(D)** = spectrum.

concretion contact, which is generally related to early diagenetic concretionary growth before compaction (Sellés-Martínez, 1996). The second group, carbonate aggregates and rosettes, encloses micrometre spherical and ellipsoidal concretions formed via replacement growth and characterised by cores of OM surrounded by outlying dolomite of the concretionary bodies (Figure 5) (Dong et al., 2008; 2013).

The formation of the first group (concretions) has been traditionally explained as the result of carbonate supersaturation in porewaters driven by the generation of bicarbonate and, therefore, high alkalinity from microbial activity around concretion nuclei in the sediments (Sellés-Martínez, 1996). Then, the nuclei were sustained during growth by a pool of inorganic bicarbonate that facilitated rapid precipitation of the concretion

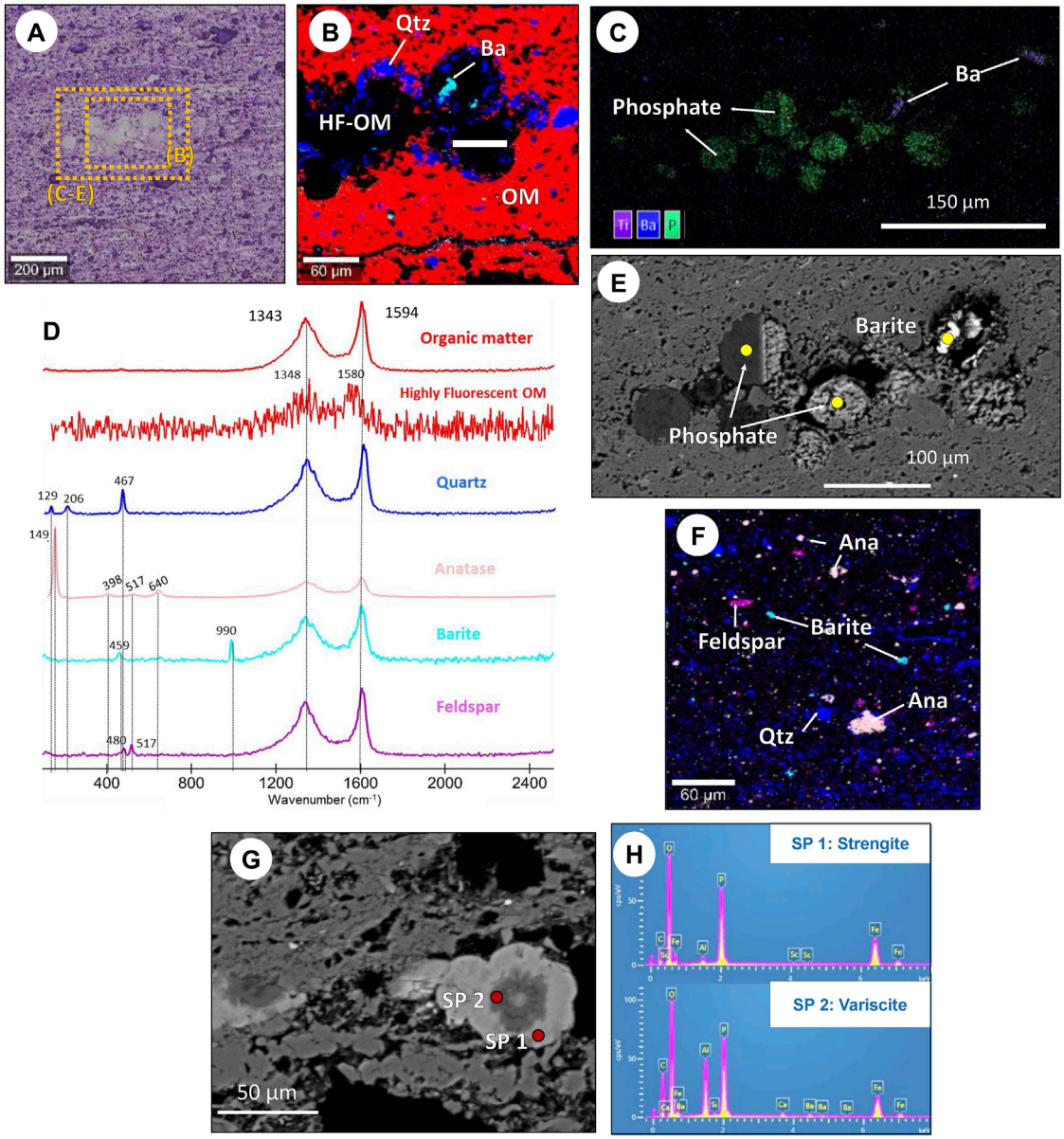

FIGURE 7
Petrographic, Raman and SEM characteristics of coccoidal microfossils in phosphatic concretions in the Zhimaping section (shelf area). **(A)** Phosphatic concretion at the top of Member IV (yellow dashed box) from the Zhimaping section (shelf lagoon). **(B)** Thin section composed of organic-rich shale with alternating pale brown and black bands **(C)** Plane polarized light image. Red arrows highlight ghostly coccoidal microfossils. **(D)** Backscattered electron image of **(B)**. **(E)** EDS spectra of quartz replacing the coccoidal microfossils and apatite in the matrix. **(F)** Raman hyperspectral image showing the apatite bands in which the coccoidal microfossils occur. **(G)** Raman hyperspectral image of coccoidal microfossils either totally or partially replaced by quartz (red arrows). The colours in the hyperspectral image correspond to the colours in the Raman spectra. **(H)** Raman spectra of **(B)** showing OM and associated minerals. SP in **(G)** = spectrum.

matrix during early diagenesis (Raiswell and Fisher, 2000; Gaines and Vorhies, 2016). Thus, the $\delta^{13}C$ of carbonate concretions generally depends on the source of carbonate ions in pore waters. As a result, $\delta^{13}C$ values of carbonate concretions are usually characterised by ^{13}C depletions relative to seawater, often used as fingerprints of specific microbial metabolic processes that trigger and maintain concretion growth (Raiswell and Fisher, 2000). However, limestone concretions with ^{13}C-enrichments in the geological record have also been attributed to methanogenesis (e.g., Birgel et al., 2015).

An alternative mechanism to form these spheroid structures has been attributed to wave action in high-energy shallow marine environments (Akin et al., 2013). However, the estimated sedimentation rates of the studies sections argue against this mechanism. In the areas where spheroidal morphologies are present, sedimentation rates are remarkably low (between 0.02 and 0.34 cm/kyr, calculated as total sediment thickness divided by total time), and shales are relatively homogeneous in granulometry. Thus, it is likely that shales were deposited below or near storm wave base, as already proposed based on other

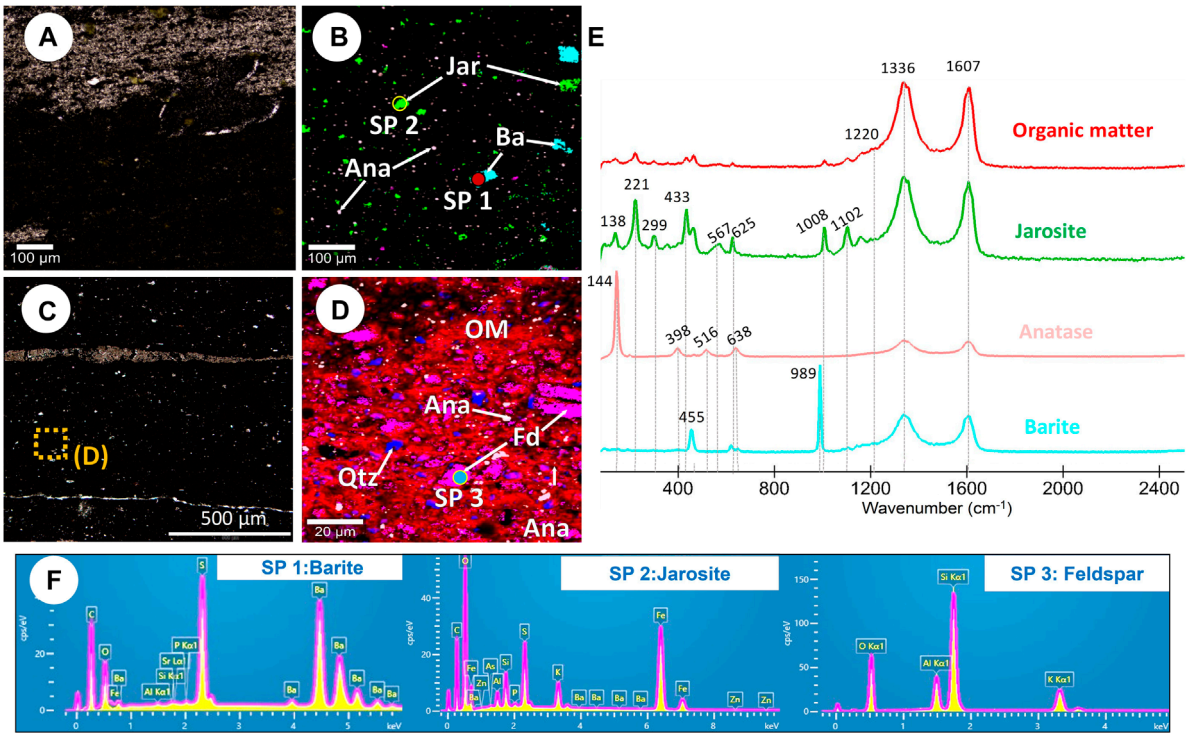

FIGURE 8
Petrographic, Raman and SEM characteristic of the Fengtan section (basin). **(A)** Thin section from the Fengtan section showing massive and dark organic-rich shale with abundant quarzitic patches. **(B)** Raman hyperspectral image of **(A)** showing isolated euhedral barite crystals and subhedral jarosite crystals. The colours in the hyperspectral image correspond to the colours in the Raman spectra. **(C)** Thin section of an organic-rich shale from a different sample in the Fentang section. **(D)** Raman hyperspectral image of **(C)** showing euhedral subhedral feldspar grains. The colours in the hyperspectral image correspond to the colours in the Raman spectra **(E)** Raman spectra of **(B)** showing OM and associated minerals. Note that spectrum of OM corresponds to image **(D)**. **(F)** EDS spectra of red circles shown in **(B,D)**. SP in **(B,D)** = spectrum.

TABLE 1 Summary table of the characteristics of the different kerogen types, including their principal Raman peaks and $\delta^{13}C_{org}$ values and mineral associations. Raman peaks and $\delta^{13}C_{org}$ are from Cañadas et al. (2022). Ap, apatite; V-S, variscite-strengite; Ba, barite; Ja, jarosite.

	Shelf lagoon	Upper slope	Lower slope	Basin
	K type A	K type C	K type A	K type B
OM	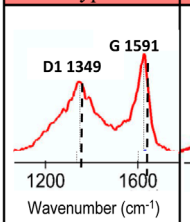	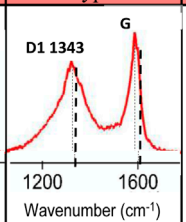	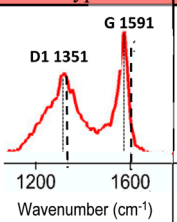	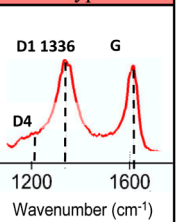
$\delta^{13}C_{org}$ (‰)	−38.6 to −34.6	−35.7 to −38.5	−32.8 to −29.8	−32.0 to −34.4
Quartz				
Dolomite				
Anatase				
Pyrite				
Phosphate	Ap	V-S		
Sulphate		Ba		Ba / Ja
Feldspar				

Ap= apatite V-S= variscite-strengite Ba= barite Ja= jarosite

TABLE 2 Summary table of OM Raman parameters, associated mineralogy and characteristics of diagenetic spheroids observed in organic-rich shales from Member IV. Classification of kerogens with spectral parameters from Cañadas et al. (2022).

			Shelf lagoon		Upper slope		Lower slope		Basin		Figure
	Kerogen type		A		C		A		B		
OM	Raman spectral parameters	D1	1349		1343		1351		1336		Figure 5J, Figure 6H, Figure 7D, Figure 8E
		G	1591		1594		1591		1607		
		D4	1245		1246		1245		1220		
		I-1350/1600	0.68		0.8		0.62		1.03		
		D-FWHM	113		120		156		100		
		G-FWHM	60		48		33		45		
Dolomite		Size	50 -100 µm	20 cm			5-20 µm (indiv) 50-150 µm (aggreg)				Figure 5A-B-C-D-E-G-H
		Morphology	Spherical and ellipsoidal rosettes	Concretion			Spheroidal or ellipsoidal rosettes, Dolomitic rims, Sparitic dolomite spheres				
Phosphate		Size	5-15 cm		50-70 µm	50 µm					Figure 6A-F, Figure 7C-E-G
		Morphology	Layered-Banded		Spheroidal	Rosettes					
		Phase	Apatite		Variscite-Strengite						
Anatase		Size	<5 µm	5-15 µm	5-15 µm		<5 µm		<5 µm	5-10 µm	Figure 5E, Figure 6G, Figure 7F, Figure 8B-D
		Morphology	Subrounded and subangular	Rounded	Isolated or forming aggregates		Subrounded and rounded		Subrounded	Rounded	
Sulphate		Size			2-10 µm				10-40 µm	20-50 µm	Figure 7B-C-F, Figure 8B
		Morphology			Subangular				Subhedral	Eu-subhedral	
		Phase			Barite				Jarosite	Barite	
Pyrite		Size	10-20 µm	5-10 µm			1- 40 µm	5-10 µm	0.25-2 mm		Figure 5B-E-G-H
		Morphology	Rounded and suhhedral	Framboidal			Eu/subhedral	Framboidal	Euhedral		
Quartz		Size	5-20 µm	5-20 µm	5-20 µm	5-20 µm	5-20 µm		up to 5 cm	200-400 µm	Figure 5B-E-G, Figure 6D-G, Figure 7B-F, Figure 8D
		Morphology	Subangular	Cocoidal	Subangular	Quarcitic rim	Subangular		Banded	Patched	
Feldspar		Size			5-30 µm				1-20 µm		Figure 8D
		Morphology			Subangular				Subhedral		

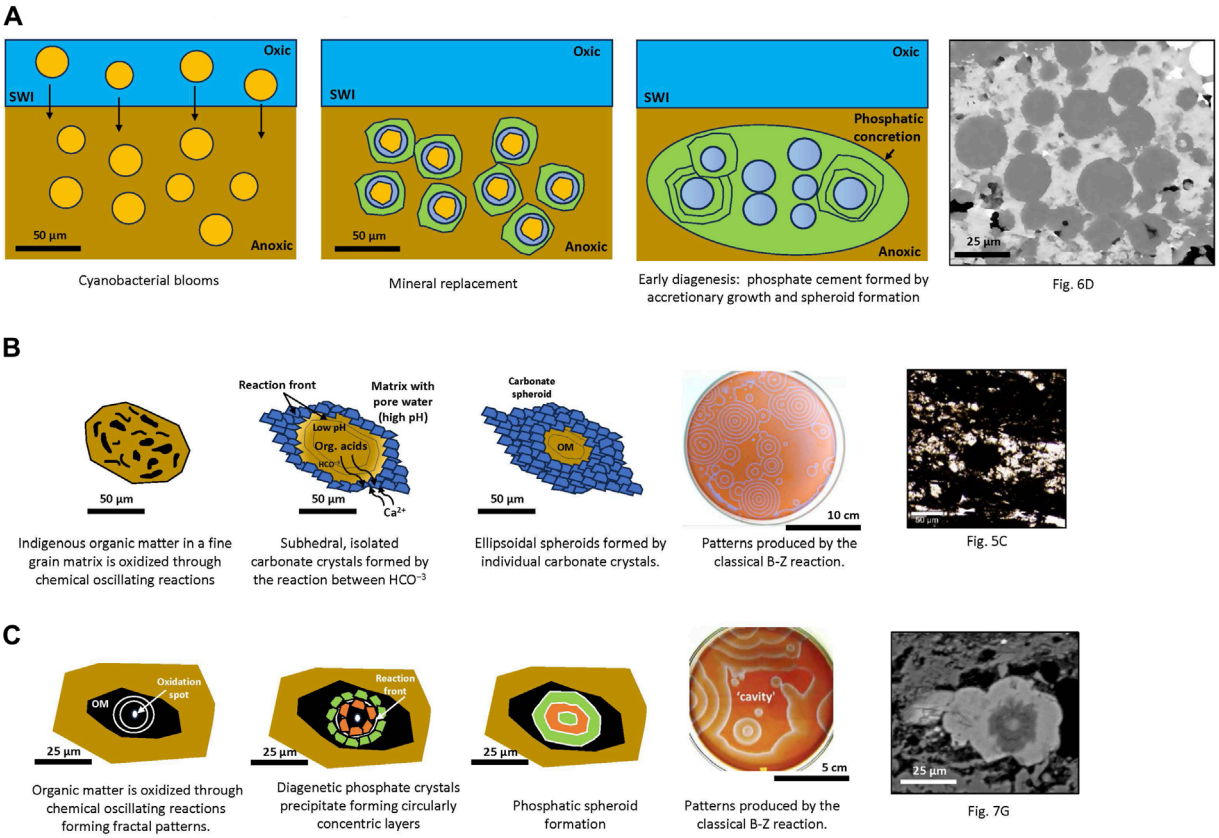

FIGURE 9
Proposed models for the diagenetic growth of investigated carbonate and phosphatic spheroids from abiotic decarboxylation of biomass. **(A)** Mineral microfossils and spheroid formation. **(B)** Abiotic carbonate diagenetic spheroid formation. **(C)** Abiotic phosphate diagenetic spheroid formation. Chemically-oscillating experiments were performed with the same chemicals as in the classical Belousov-Zhabotinsky experiment (see Papineau et al., 2017 for experimental details). SWI: sediment water interface; OM: organic matter.

sedimentological evidence such as planar laminations and only rare intraclasts (McFadden et al., 2008), where slow-moving currents prevented coarse-grained sediment from migrating into low-energy depositional environments. These observations are inconsistent with a high-energy environment; therefore, the wave agitation model is not considered a potential mechanism of concretion formation in this study.

The formation of the second group (aggregates and rosettes) has been attributed to possible gas bubbles produced by oxygenic phototrophs in microbial mats and stromatolites (Bosak et al., 2010; Sallstedt et al., 2018), gas bubbles replaced by carbonate formed by microbial decomposition of OM and anaerobic oxidation of methane near the sediment-water interface (Dong et al., 2008) or microbial biomass replaced by carbonate precipitation under slightly alkaline conditions (Varkouhi et al., 2022). In all cases, gases from OM decomposition would have created cavities or bubbles subsequently filled by carbonate precipitated from anaerobic methane oxidation. However, as explained next, gas bubbles from organisms or OM decomposition are not exclusive mechanisms to form concretions.

The conventional characteristics of carbonate concretions are that they preferentially occur in organic-rich mudstones, where the decomposition of OM facilitates the continuous supply of bicarbonate in pore water, and that they are formed at shallow depths during the early stages of diagenesis (Sellés-Martínez, 1996; Raiswell and Fisher, 2000). However, ellipsoidal carbonate concretions have been reported in organic-poor glacial deposits (Vuillemin et al., 2013), organic-poor mudstones (Gaines and Vorhies, 2016) and organic-poor green silty shale (Liu A. Q. et al., 2019), indicating that concretion growth may be sustained even under limited organic content conditions. In addition, the decomposition of OM and anaerobic oxidation of produced gases do not explain relevant attributes of concretions, such as their spherical to ellipsoidal concentricity with sharp boundaries or the factors that terminate concretion growth. To further understand these questions, an alternative model of formation for diagenetic concretions must include biological and abiotic processes, or a combination of both because they are not mutually exclusive and because diagenesis involves both microbial and physico-chemical processes. Indeed, abiotic processes could have played a significant role in forming diagenetic concretions in Member IV.

5.2 Phosphatic spheroids

Phosphate spheroids in organic-rich shales commonly form during very early diagenesis, allowing the preservation of original

depositional materials such as fossils and other sedimentological features (Raiswell and Fisher, 2000). This could be the case for the morphologies found in the shelf lagoon (Zhimaping) area that resemble coccoidal cyanobacterial mats (Figures 6C, D, F) or the upper slope (Taoying) with characteristic organic-rich spheroidal and rosette morphologies (Figures 7A–C, E, G). The coccoidal cyanobacterial mats are enclosed in phosphatic concretions (Figure 6A) and present an excellent level of preservation of these objects, indicating that the growth of phosphate concretions occurred during early diagenesis. Lastly, the two different spheroidal morphologies in Taoying, organic-rich spheroidal and rosettes, likely have different origins as the former also resembles cyanobacteria-like microfossils (Figures 7B, C, E) with a phosphatic core whose origin could be attributed to microfossil replacement by phosphate precipitation, and the latter present concentric laminations whose origin could be attributed to COR (Figure 7G) as discussed in the next section.

One may argue that an abiotic origin of the coccoidal morphologies, such as grains partially silicified due to compaction, cannot be ruled out. However, the homogeneous morphology and sizes, with average values of 9.7 ± 3.2 μm, spatial organisation within a phosphatic concretion and chemical composition, and the geochemical context in which they formed support the interpretation that they are likely fossils. Also, while coccoidal microfossils are typically aggregated (e.g., She et al., 2013), they can occur as individual spheres scattered across a bed. For example, similar fossils of colonial coccoidal cyanobacteria preserved as individual spheres with similar sizes were reported in Silurian organic-rich cherts (Kremer, 2006), Mesoproterozoic stromatolites (Golubic and Seong-Joo, 1999) and late Devonian benthic cyanobacterial mats (Kazmierczak et al., 2012), which are compared to modern coccoid cyanobacteria (Chroococcus). These studies suggested that cyanobacteria and algal biomass were the dominant microbial population of large blooms and formed macroaggregates that rapidly sank to the seafloor and were overgrown by benthic coccoidal cyanobacterial mats. In such a dynamic scenario, the decomposition of biomass would release phosphate during shallow burial that would have favoured early diagenetic phosphatisation as calcium, barium, iron cations, and halogens were available in pore water. Interestingly, the occurrence of apatite bands (Figure 6), iron-rich phosphate phases (Figure 7) and large barite grains associated with phosphates (Figure 7F) described in this study suggest that the abiotic decomposition of biomass may have also played a key role in the formation of these mineral phases in Member IV (more in the next section).

In South China, coccoidal microfossils have been previously reported in phosphorites of the Doushantuo Fm. (Xiao, 2004; Muscente et al., 2015), located in the same proximal environments as those in the present study. Similarly to the microfossils found in Member IV, the well-preserved cellular structures reported in these studies suggest phosphatisation occurred immediately after deposition. Different P sources likely accounted for the accumulation and preservation of apatite. This is because, during the Ediacaran, continental weathering and P remineralisation were the principal sources of phosphorus in the environment (Laakso et al., 2020; Dodd et al., 2023), which favoured the extensive production of OM (Cañadas et al., 2022) and the proliferation of microbial communities (She et al., 2013), like the coccoidal cyanobacteria shown in Figure 6. The organic decay of these microbial communities during burial caused the release of P remineralised from OM, probably via bacteria sulfate reduction. The redox conditions that prevailed during Member IV deposition in the Ediacaran oceans, with increasing oxic conditions in the shallow water column and anoxic (or euxinic) conditions dominating in the deep basin (Cañadas et al., 2022; Li et al., 2024) promoted iron-(oxyhydr)oxide (FeOOH) particulates to efficiently adsorb dissolved phosphate and transported the Fe-bound phosphorous ($FeOOH{\cdot}PO_4$) into marine sediments, ultimately precipitating as diagenetic apatite bands and phosphorite deposits (Cui et al., 2015; 2016).

Phosphatic spheroids and rosettes occur in organic-rich laminated horizons at Zhimaping and Taoying sections (Figures 7A–D, G). However, although these spheroids have been previously reported to occur in black shales (Kidder et al., 2003), they are more commonly associated with other lithologies such as carbonates and chert (Mossman et al., 2005; Papineau et al., 2016). The occurrence of apatite spheroids and rosettes in organic-rich sediments from proximal environments is consistent with a phosphorus-rich environment that stimulated a high level of primary productivity (Cañadas et al., 2022), similarly as described for Member II (She et al., 2013; She et al., 2014) and the stromatolitic phosphorite from the late Paleoproterozoic Aravalli Supergroup (Papineau et al., 2016). Zhimaping and Taoying are located in proximal areas where carbon and nitrogen isotope studies suggest high photoautotrophic production (Cañadas et al., 2022) and, together with the excellent preservation of microfossils, suggest the influence of microorganisms during phosphogenesis.

5.3 An abiotic model for the formation of diagenetic spheroids

The spherical and ellipsoidal morphologies of the spheroids shown in Figure 5 and the concentric layered pattern observed in Figure 7G resemble the circularly concentric and radially patterned structures previously described as 'diagenetic spheroids' (Papineau et al., 2016; 2017; 2021; Dodd et al., 2018; Papineau, 2020; Gabriel et al., 2021; Goodwin and Papineau, 2022). For all these examples of diagenetic spheroids, diagenetic oxidation of OM through out-of-equilibrium reactions has been proposed as the principal mechanism of pattern formation with circularly concentric layers. In addition, these examples of diagenetic spheroids present similar sizes, generally between 100 and 200 μm, and mineral assemblages that commonly include ^{13}C-depleted carbonate, ferric-ferrous, and phosphate phases mixed with OM and sulphide.

Evidence for the diagenetic oxidation of OM in Member IV is seen in the systematically negative $\delta^{13}C_{carb}$ values down to −8‰ and coeval $\delta^{13}C_{org}$ down to −39‰ (Figure 2B) (Cañadas et al., 2022). Hence, a ^{13}C-depleted oxidised source of OM was assimilated by authigenic carbonate and phosphate in Member IV. Furthermore, the core characteristic of the different spheroids described in the organic-rich shales of Member IV is that OM is a ubiquitous primary component. Hence, it is reasonable to propose that OM played a relevant role in forming these diagenetic spheroidal structures.

In this regard, the degradation of OM occurs through different reactions depending on the diagenetic stage. Thus, in the early stages of diagenesis, OM releases free carboxylic acids containing new metabolic intermediates that other organisms readily use. This process occurs through biotic decarboxylation reactions, such as Tricarboxylic Acid Cycle (TCA cycle), sulfate reduction and fermentation. As diagenesis progresses, carboxylic acids decompose abiotically via decarboxylation reactions to form CO_2. Finally, during late diagenesis, abiotic decarboxylation becomes the principal process that produces CO_2, ultimately contributing to carbonate and phosphate supersaturation for precipitation and concretionary growth.

5.3.1 Chemical oscillating reactions (COR) for spheroid formation

Among the abiotic decarboxylation reactions that take part in the diagenetic oxidation of OM, COR represent an abiotic mechanism of pattern formation that can explain the spheroidal to the ellipsoidal concentric and radial alignment of crystals in rosette-like morphologies found in the shelf lagoon (Figure 5) and slope sections (Figure 7). The classical COR is the Belousov-Zhabotinsky (BZ) reaction which consists of out-of-equilibrium oxidation of the carboxylic acid malonate [$CH_2(COOH)_2$] with strong halogen oxidants such as bromate (BrO_3^-) and iodate (IO_3^-), as well as with a strong acid such as sulfuric (H_2SO_4) acid to produce CO_2 (Zhabotinsky, 1991). As a result, COR produce characteristic circularly concentric geometric patterns that diffuse radially. Papineau et al. (2017) reproduced COR using the same chemicals as the classical Belousov-Zhabotinsky experiment and obtained oxidation spots and concentric oxidation fronts with rounded equidistant lines, curved equidistant lines forming twins and eventually cavity patterns, single spot patterns, and CO_2 bubbles.

Environmental conditions during the late Ediacaran could have facilitated spontaneous COR in the subsurface as the principal ingredients for these reactions to occur could have been supplied from different sources. First, carboxylic acids would have been sourced from dynamic organic carbon fluxes to sediments facilitating the preservation of widespread deposits of OM in the Doushantuo Fm., especially during the late Ediacaran Member IV (Cañadas et al., 2022). In such a scenario, microbial decomposition of sinking OM in the water column and the water-sediment interface likely drove the release of abundant carboxylic acids that ultimately fuelled the proposed COR. Secondly, strong acids (sulphuric and phosphoric acid) would be derived from sulfur and phosphorus contents, two particularly abundant elements during the deposition of Member IV. Seawater sulfate concentrations could have increased from <1 mM to 6–10 mM (Blättler et al., 2020). In turn, the high sulfur content in the global Ediacaran Ocean would lead to phosphorus remineralisation mediated by sulfate-reducing bacteria (Laakso et al., 2020). Lastly, strong oxidants (iodate and bromate) would be observed from high I/(Ca + Mg), which has been used as evidence for increased ocean oxygenation during the Paleo- and Neoproterozoic (Hardisty et al., 2017; Lu et al., 2017). This is consistent with recent studies about iodine concentrations (Wei et al., 2019) in the Doushantuo Fm. that show two minor I/(Ca + Mg) increases at the basal and middle part of the Doushantuo Formation, and a large I/(Ca + Mg) increase described in the uppermost Doushantuo Fm. (Member IV), which suggests significant ocean oxygenation of the water column. On the other hand, algae and cyanobacteria can also concentrate iodine and bromine (Gribble, 2000; Carpenter, 2003). These primary producers produce brominated and iodinated intermediates that decay to release organo-bromine and organo-iodine compounds.

It is worth mentioning that the occurrence of carbonate and phosphatic spheroids in this study is only observed in sections (Zhimaping, Taoying and Xiajiaomeng) located in areas with carbon and nitrogen isotope signatures most consistent with high primary production (Cañadas et al., 2022), thus with abundant OM that could have played a significant role in the formation of diagenetic spheroids. Additionally, diagenetic spheroids formed via abiotic oxidation of biomass commonly include ^{13}C-depleted carbonates (Dodd et al., 2018; Papineau, 2020). In this regard, systematic ^{13}C-depleted carbonates were reported in samples from the Doushantuo Fm. (McFadden et al., 2008; Zhu et al., 2013), including concretions with values as low as −11‰ in shallow areas (Dong et al., 2008) and −14‰ in basinal sections (Jiang et al., 2011), which are consistent with the addition of ^{13}C-depleted carbon from biomass, which is common in the studied samples with values down to −39‰ (McFadden et al., 2008; Cañadas et al., 2022).

It is generally known that sulfate inhibits dolomite precipitation (Compton, 1988), although bacterial sulfate reduction has been related to dolomite precipitation (Baldermann et al., 2015). It is likely that cementation began during concretion growth and continued after sulfate was exhausted from pore water, promoting the precipitation of dolomite concretions. This could explain why sulfates are absent in Zhimaping and Xiajiomeng sections, but sulfides are present. The traditional mechanism of concretion formation would have implied alkaline conditions typically associated with sulfate reduction in the sediments to favour carbonate precipitation. However, abiotic precipitation of proto-dolomite has been recently reported as an alternative abiotic mechanism of dolomite formation (Liu et al., 2019). In this recent study, experiments demonstrate that negatively charged clay minerals such as illite and montmorillonite aid the precipitation of abiotic proto-dolomite under ambient conditions, possibly via electrostatic binding hydroxylated Mg^{2+} and Ca^{2+}. This is important because illite or mixtures of illite/smectite compositions have been reported as the only clays present in Member IV shales, where illite is dominant (Bristow et al., 2009) and could thus have contributed to a favourable scenario for abiotic dolomite precipitation. Moreover, carboxylic acids from microbes or their decomposed products have recently been identified as a crucial functional group that facilitates the binding of Ca^{2+} and Mg^{2+} during Ca-Mg carbonate growth (Qiu et al., 2017) and serves as independent evidence of abiotic mechanisms of carbonate precipitation.

Identifying morphologies and textures resulting from abiotic mineral precipitation is particularly problematic because of the ubiquitous presence of biological compounds within. In this context, COR may be viewed as an alternative abiotic mechanism capable of producing rounded and concentric patterns of carbonate composition due to radially expanding circular waves of diagenetic oxidation products. In Figure 9, we proposed three different models for the diagenetic growth of investigated carbonate and phosphatic spheroids from abiotic decarboxylation of biomass. In the first model (Figure 9A), 'Mineral microfossils and spheroid formation',

the cyanobacterial bloom is produced and phosphate is rapidly precipitated from settled OM at the sediment-water interface (SWI). Then, mineral replacement takes place through aerobic respiration of bacteria which gradually lowers pH causing silica to precipitate and replace the organic coccoid. Limited O_2 production at the seafloor, along with bacteria sulfate reducers created a redox geochemical gradient and elevated phosphate concentrations that led to phosphate precipitation around the cyanobacteria. During early diagenesis, concentric and asymmetric zonings of phosphate cement formed by accretionary growth resulting in a phosphatic ellipsoidal diagenetic spheroid (see Figure 6A).

In the second model (Figure 9B), 'Abiotic carbonate diagenetic spheroid formation', indigenous organic matter in a fine grain matrix is oxidized through chemical oscillating reactions. Generation and diffusion of oxidation spots form subhedral, isolated carbonate crystals by the reaction between HCO^{-3}, a byproduct from the breakdown of organic acids originating from the dead organism and pore-water Ca, which was mostly derived from the surrounding matrix outside the concretion. Then, circular patterns following the expansion of oxidation spots are formed. Precipitation of carbonate at the reaction front forms ellipsoidal spheroids formed by individual carbonate crystals. Patterns are produced by the classical B-Z reaction whereby oxidation spots and concentric oxidation fronts are formed with characteristic rounded equidistant lines. Lastly, in the third model, 'Abiotic phosphate diagenetic spheroid formation', organic matter aggregates in a -Si and P-rich fine grain matrix are oxidized through chemical oscillating reactions. Oxidation spots form during the decay of OM triggering the formation of fractal patterns. The oxidation spot expands the precipitated diagenetic phosphate crystals into circularly concentric layers. Full oxidation of OM and formation of the phosphatic circular spheroid. Patterns are produced by the classical B-Z reaction whereby curved lines form a 'cavity' that encloses concentric oxidation spots.

Mineral assemblages described in Member IV diagenetic spheroids formed by quartz, apatite, carbonate, OM, pyrite, anatase, and ferric-ferrous oxides are commonly associated with diagenetic spheroids (Papineau et al., 2017; Dodd et al., 2018; Papineau, 2020; Gabriel et al., 2021). The study Member IV diagenetic spheroids are thus consistent with the early diagenetic oxidation of microbial biomass and provide a plausible link to COR as an abiotic mechanism for forming spheroids in the early diagenetic environment of these organic-rich shales.

6 Conclusion

New Raman spectroscopy and SEM on organic-rich shales of Member IV of the Doushantuo Fm. reveal the occurrence of diagenetic spheroids consistent with biotic and abiotic interactions during its formation. Primary photosynthetic production and OM remineralization processes are evidenced by dolomitic or phosphate spheroids of various sizes enclosing circularly concentric OM and coccoidal microfossils hosted in spheroidal phosphatic spheroids in sedimentary layers. However, the formation of the described spheroids is consistent with the early diagenetic oxidation of microbial biomass and provides a plausible link to COR as an abiotic mechanism for forming spheroids in the early diagenetic environment of these organic-rich shales. This is particularly evident in the occurrence of OM with spheroidal structures intimately associated with minerals like quartz, apatite, ^{13}C-depleted carbonate, OM, pyrite, anatase, and ferric-ferrous oxides. This mineral assemblage is commonly found in abiotic diagenetic spheroids, suggesting a close interaction between photosynthetic biomass production and the reactants and products associated with chemically oscillating reactions (COR) that underpin the formation of these spheroids. The diagenetic oxidation of OM was, in part, abiotic, but it was facilitated by microbial communities within a context of sustained primary production. The diagenetic alteration of OM was also influenced abiotically by COR, which explains the circularly concentric spheroidal to ellipsoidal concretions and rosettes in Member IV of the Doushantuo Fm. The co-occurrence of biotic and abiotic signatures in the sedimentary record, particularly in the context of a planet's early history, could inform the search for life on planets with similar environmental conditions.

Data availability statement

The original contributions presented in the study are included in the article. Further inquiries can be directed to the corresponding author.

Author contributions

FC: Conceptualization, Formal Analysis, Funding acquisition, Investigation, Methodology, Project administration, Software, Visualization, Writing–original draft, Writing–review and editing. DP: Methodology, Software, Supervision, Writing–review and editing, Validation. ZS: Writing–review and editing, Validation.

Funding

The author(s) declare that financial support was received for the research, authorship, and/or publication of this article. FC acknowledges support from NERC for a DTP scholarship (NE/L002485/1).

Acknowledgments

In addition, we thank J. Davy and T. Gregory for their assistance with polishing thin sections and with SEM-EDS analyses, respectively. The following are also thanked for their contributions to the field trips and sample collection: G. Shields, S. Poulton, M. Zhu, H. Ling, Xi Chen, Da Li, M. Chen and Z. Tian.

Conflict of interest

The authors declare that the research was conducted in the absence of any commercial or financial relationships that could be construed as a potential conflict of interest.

Publisher's note

References

Akin, S., Pufahl, P., Hiatt, E., and Pirajno, F. (2013). Oxygenation of shallow marine environments and chemical sedimentation in Palaeoproterozoic peritidal settings: frere Formation, Western Australia. *Sedimentology* 60, 1559–1582. doi:10.1111/sed.12038

An, Z., Jiang, G., Tong, J., Tian, L., Ye, Q., Song, H. H., et al. (2015). Stratigraphic position of the Ediacaran Miaohe biota and its constrains on the age of the upper Doushantuo δ13C anomaly in the Yangtze Gorges area, South China. *Precambrian Res.* 271, 243–253. doi:10.1016/j.precamres.2015.10.007

Baldermann, A., Deditius, A. P., Dietzel, M., Fichtner, V., Fischer, C., Hippler, D., et al. (2015). The role of bacterial sulfate reduction during dolomite precipitation: implications from Upper Jurassic platform carbonates. *Chem. Geol.* 412, 1–14. doi:10.1016/j.chemgeo.2015.07.020

Ball, P. (2012). Pattern Formation in nature: physical constraints and self-organising characteristics. *Arch. Des.* 82, 22–27. doi:10.1002/ad.1375

Berner, R. A. (1968). Calcium carbonate concretions formed by the decomposition of organic matter. *Sci.* (80) 159, 195–197. doi:10.1126/science.159.3811.195

Birgel, D., Meister, P., Lundberg, R., Horath, T. D., Bontognali, T. R. R., Bahniuk, A. M., et al. (2015). Methanogenesis produces strong 13C enrichment in stromatolites of Lagoa Salgada, Brazil: a modern analogue for Palaeo-/Neoproterozoic stromatolites? *Geobiology* 13, 245–266. doi:10.1111/gbi.12130

Blättler, C. L., Bergmann, K. D., Kah, L. C., Gómez-Pérez, I., and Higgins, J. A. (2020). Constraints on Meso-to Neoproterozoic seawater from ancient evaporite deposits. *Earth Planet. Sci. Lett.* 532, 115951. doi:10.1016/j.epsl.2019.115951

Bosak, T., Bush, J. W. M., Flynn, M. R., Liang, B., Ono, S., Petroff, A. P., et al. (2010). Formation and stability of oxygen-rich bubbles that shape photosynthetic mats. *Geobiology* 8, 45–55. doi:10.1111/j.1472-4669.2009.00227.x

Breheret, J.-G. (1991). Phosphatic concretions in black facies of the Aptian-Albian Marnes bleues Formation of the Vocontian basin (SE France), and at site DSDP 369: evidence of benthic microbial activity. *Cretac. Res.* 12, 411–435. doi:10.1016/0195-6671(91)90018-8

Bristow, T. F., Kennedy, M. J., Derkowski, A., Droser, M. L., Jiang, G., and Creaser, R. A. (2009). Mineralogical constraints on the paleoenvironments of the ediacaran Doushantuo Formation. *Proc. Natl. Acad. Sci. U. S. A.* 106, 13190–13195. doi:10.1073/pnas.0901080106

Cañadas, F., Papineau, D., Leng, M. J., and Li, C. (2022). Extensive primary production promoted the recovery of the Ediacaran Shuram excursion. *Nat. Commun.* 13, 148–149. doi:10.1038/s41467-021-27812-5

Carpenter, L. J. (2003). Iodine in the marine boundary layer. *Chem. Rev.* 103, 4953–4962. doi:10.1021/cr0206465

Compton, J. S. (1988). Degree of supersaturation and precipitation of organogenic dolomite. *Geology* 16, 318–321. doi:10.1130/0091-7613(1988)016<0318:DOSAPO>2.3.CO;2

Cui, H., Kaufman, A. J., Xiao, S., Peek, S., Cao, H., Min, X., et al. (2016). Environmental context for the terminal Ediacaran biomineralization of animals. *Geobiology* 14, 344–363. doi:10.1111/gbi.12178

Cui, H., Kaufman, A. J., Xiao, S., Zhu, M., Zhou, C., and Liu, X. M. (2015). Redox architecture of an Ediacaran Ocean margin: integrated chemostratigraphic ($\delta^{13}C$-$\delta^{34}S$-$^{87}Sr/^{86}Sr$-Ce/Ce*) correlation of the Doushantuo Formation, south China. *Chem. Geol.* 405, 48–62. doi:10.1016/j.chemgeo.2015.04.009

Dodd, M. S., Papineau, D., She, Z., Fogel, M. L., Nederbragt, S., and Pirajno, F. (2018). Organic remains in late Palaeoproterozoic granular iron formations and implications for the origin of granules. *Precambrian Res.* 310, 133–152. doi:10.1016/j.precamres.2018.02.016

Dodd, M. S., Shi, W., Li, C., Zhang, Z., Cheng, M., Gu, H., et al. (2023). Uncovering the Ediacaran phosphorus cycle. *Nature* 618, 974–980. doi:10.1038/s41586-023-06077-6

Dong, J., Zhang, S., Jiang, G., Li, H., and Gao, R. (2013). Greigite from carbonate concretions of the ediacaran Doushantuo Formation in south China and its environmental implications. *Precambrian Res.* 225, 77–85. doi:10.1016/j.precamres.2012.03.010

Dong, J., Zhang, S. H., Jiang, G. Q., Zhao, Q.Le, Li, H. Y., Shi, X. Y., et al. (2008). Early diagenetic growth of carbonate concretions in the upper Doushantuo Formation in South China and their significance for the assessment of hydrocarbon source rock. *Sci. China, Ser. D. Earth Sci.* 51, 1330–1339. doi:10.1007/s11430-008-0107-3

Duck, R. W. (1995). Subaqueous shrinkage cracks and early sediment fabrics preserved in Pleistocene calcareous concretions. *J. Geol. Soc. Lond.* 152, 151 LP–156. doi:10.1144/gsjgs.152.1.0151

El Kabouri, J., Errami, E., Becker-Kerber, B., Ennih, N., Linnemann, U., Fellah, C., et al. (2023). Ediacaran biota from ougnat massif (eastern anti-atlas, Morocco): paleoenvironmental and stratigraphic constraints. *J. Afr. Earth Sci.* 198, 104806. doi:10.1016/j.jafrearsci.2022.104806

Furuyama, S., Kano, A., Kunimitsu, Y., Ishikawa, T., Wang, W., and Liu, X. C. (2017). Chemostratigraphy of the Ediacaran basinal setting on the Yangtze platform, South China: oceanographic and diagenetic aspects of the carbon isotopic depth gradient. *Isl. Arc* 26, 1–14. doi:10.1111/iar.12196

Gabriel, N. W., Papineau, D., She, Z., Leider, A., and Fogel, M. L. (2021). Organic diagenesis in stromatolitic dolomite and chert from the late Palaeoproterozoic McLeary Formation. *Precambrian Res.* 354, 106052. doi:10.1016/j.precamres.2020.106052

Gaines, R. R., and Vorhies, J. S. (2016). Growth mechanisms and geochemistry of carbonate concretions from the Cambrian Wheeler Formation (Utah, USA). *Sedimentology* 63, 662–698. doi:10.1111/sed.12234

Golubic, S., and Seong-Joo, L. (1999). Early cyanobacterial fossil record: preservation, palaeoenvironments and identification. *Eur. J. Phycol.* 34, 339–348. doi:10.1080/09670269910001736402

Gómez-Peral, L. E., Kaufman, A. J., and Poiré, D. G. (2014). Paleoenvironmental implications of two phosphogenic events in Neoproterozoic sedimentary successions of the Tandilia System, Argentina. *Precambrian Res.* 252, 88–106. doi:10.1016/j.precamres.2014.07.009

Goodwin, A., and Papineau, D. (2022). Biosignatures associated with organic matter in late paleoproterozoic stromatolitic dolomite and implications for martian carbonates. *Astrobiology* 22, 49–74. doi:10.1089/ast.2021.0010

Gribble, G. W. (2000). The natural production of organobromine compounds. *Environ. Sci. Pollut. Res.* 7, 37–49. doi:10.1065/espr199910.002

Hardisty, D. S., Lu, Z., Bekker, A., Diamond, C. W., Gill, B. C., Jiang, G., et al. (2017). Perspectives on Proterozoic surface ocean redox from iodine contents in ancient and recent carbonate. *Earth Planet. Sci. Lett.* 463, 159–170. doi:10.1016/j.epsl.2017.01.032

Jiang, G., Kaufman, A. J., Christie-Blick, N., Zhang, S., and Wu, H. (2007). Carbon isotope variability across the Ediacaran Yangtze platform in South China: implications for a large surface-to-deep ocean δ13C gradient. *Earth Planet. Sci. Lett.* 261, 303–320. doi:10.1016/j.epsl.2007.07.009

Jiang, G., Shi, X., Zhang, S., Wang, Y., and Xiao, S. (2011). Stratigraphy and paleogeography of the ediacaran Doushantuo Formation (ca. 635–551Ma) in South China. *Gondwana Res.* 19, 831–849. doi:10.1016/j.gr.2011.01.006

Kazmierczak, J., Kremer, B., and Racki, G. (2012). Late Devonian marine anoxia challenged by benthic cyanobacterial mats. *Geobiology* 10, 371–383. doi:10.1111/j.1472-4669.2012.00339.x

Kenward, P., Ueshima, M., Fowle, D., Goldstein, R., Gonzalez, L., and Roberts, J. (2013). Ordered low-temperature dolomite mediated by carboxyl-group density of microbial cell walls. *Am. Assoc. Pet. Geol. Bull.* 97, 2113–2125. doi:10.1306/05171312168

Kidder, D. L., Krishnaswamy, R., and Mapes, R. H. (2003). Elemental mobility in phosphatic shales during concretion growth and implications for provenance analysis. *Chem. Geol.* 198, 335–353. doi:10.1016/S0009-2541(03)00036-6

Kitanaka, R., Tsuboi, M., and Ozaki, Y. (2023). Biogenic apatite in carbonate concretions with and without fossils investigated *in situ* by micro-Raman spectroscopy. *Sci. Rep.* 13, 9714. doi:10.1038/s41598-023-36566-7

Kremer, B. (2005). Mazuelloids: product of post-mortem phosphatization of acanthomorphic acritarchs. *Palaios* 20, 27–36. doi:10.2110/palo.2003.p03-112

Kremer, B. (2006). Mat-forming coccoid cyanobacteria from early Silurian marine deposits of Sudetes, Poland. *Acta Palaeontol. Pol.* 51, 143–154.

Laakso, T. A., Sperling, E. A., Johnston, D. T., and Knoll, A. H. (2020). Ediacaran reorganization of the marine phosphorus cycle. *Proc. Natl. Acad. Sci.* 117, 11961–11967. doi:10.1073/pnas.1916738117

Li, R., Zhou, X., Eddy, M. P., Ickert, R. B., Wang, Z., Tang, D., et al. (2024). Stratigraphic evidence for a major unconformity within the Ediacaran System. *Earth Planet. Sci. Lett.* 636, 118715. doi:10.1016/j.epsl.2024.118715

Liu, A. Q., Tang, D. J., Shi, X. Y., Zhou, L. M., Zhou, X. Q., Shang, M. H., et al. (2019a). Growth mechanisms and environmental implications of carbonate concretions from the

~ 1.4 Ga Xiamaling Formation, North China. *J. Palaeogeogr.* 8, 20. doi:10.1186/s42501-019-0036-4

Liu, D., Xu, Y., Papineau, D., Yu, N., Fan, Q., Qiu, X., et al. (2019b). Experimental evidence for abiotic formation of low-temperature proto-dolomite facilitated by clay minerals. *Geochim. Cosmochim. Acta* 247, 83–95. doi:10.1016/j.gca.2018.12.036

Lu, M., Zhu, M., Zhang, J., Shields-Zhou, G. A., Li, G., Zhao, F., et al. (2013). The DOUNCE event at the top of the Ediacaran Doushantuo Formation, South China: broad stratigraphic occurrence and non-diagenetic origin. *Precambrian Res.* 225, 86–109. doi:10.1016/j.precamres.2011.10.018

Lu, W., Wörndle, S., Halverson, G. P., Zhou, X., Bekker, A., Rainbird, R. H., et al. (2017). Iodine proxy evidence for increased ocean oxygenation during the Bitter Springs Anomaly. *Geochem. Perspect. Lett.* 5, 53–57. doi:10.7185/geochemlet.1746

McFadden, K. A., Huang, J., Chu, X., Jiang, G., Kaufman, A. J., Zhou, C., et al. (2008). Pulsed oxidation and biological evolution in the ediacaran Doushantuo Formation. *Proc. Natl. Acad. Sci.* 105 (9), 3197–3202. doi:10.1073/pnas.0708336105

Mossman, D. J., Gauthier-Lafaye, F., and Jackson, S. E. (2005). Black shales, organic matter, ore genesis and hydrocarbon generation in the Paleoproterozoic Franceville Series, Gabon. *Precambrian Res.* 137, 253–272. doi:10.1016/j.precamres.2005.03.005

Muscente, A. D., Hawkins, A. D., and Xiao, S. (2015). Fossil preservation through phosphatization and silicification in the Ediacaran Doushantuo Formation (South China): a comparative synthesis. *Palaeogeogr. Palaeoclimatol. Palaeoecol.* 434, 46–62. doi:10.1016/j.palaeo.2014.10.013

Papineau, D. (2020). Chemically oscillating reactions in the formation of botryoidal malachite. *Am. Mineral.* 105, 447–454. doi:10.2138/am-2020-7029

Papineau, D., De Gregorio, B., Fearn, S., Kilcoyne, D., Mcmahon, G., Purohit, R., et al. (2016). Nanoscale petrographic and geochemical insights on the origin of the Palaeoproterozoic stromatolitic phosphorites from Aravalli Supergroup, India. *Geobiology* 14, 3–32. doi:10.1111/gbi.12164

Papineau, D., She, Z., and Dodd, M. S. (2017). Chemically-oscillating reactions during the diagenetic oxidation of organic matter and in the formation of granules in late Palaeoproterozoic chert from Lake Superior. *Chem. Geol.* 470, 33–54. doi:10.1016/j.chemgeo.2017.08.021

Papineau, D., Yin, J., Devine, K. G., Liu, D., and She, Z. (2021). Chemically oscillating reactions during the diagenetic formation of ediacaran siliceous and carbonate botryoids. *Minerals* 11, 1060. doi:10.3390/min11101060

Qiu, X., Wang, H., Yao, Y., and Duan, Y. (2017). High salinity facilitates dolomite precipitation mediated by Haloferax volcanii DS52. *Earth Planet. Sci. Lett.* 472, 197–205. doi:10.1016/j.epsl.2017.05.018

Raiswell, R., and Fisher, Q. J. (2000). Mudrock-hosted carbonate concretions: a review of growth mechanisms and their influence on chemical and isotopic composition. *J. Geol. Soc. Lond.* 157, 239 LP–251. doi:10.1144/jgs.157.1.239

Sallstedt, T., Bengtson, S., Broman, C., Crill, P. M., and Canfield, D. E. (2018). Evidence of oxygenic phototrophy in ancient phosphatic stromatolites from the Paleoproterozoic Vindhyan and Aravalli Supergroups, India. *Geobiology* 16, 139–159. doi:10.1111/gbi.12274

Sellés-Martínez, J. (1996). Concretion morphology, classification and genesis. *Earth-Science Rev.* 41, 177–210. doi:10.1016/s0012-8252(96)00022-0

She, Z., Strother, P., Mcmahon, G., Nittler, L. R., Wang, J., Zhang, J., et al. (2013). Terminal Proterozoic cyanobacterial blooms and phosphogenesis documented by the Doushantuo granular phosphorites I: *in situ* micro-analysis of textures and composition. *Precambrian Res.* 235, 20–35. doi:10.1016/j.precamres.2013.05.011

She, Z., Strother, P., Papineau, D., et al. (2014). Terminal Proterozoic cyanobacterial blooms and phosphogenesis documented by the Doushantuo granular phosphorites II: microbial diversity and C isotopes. *Precambrian Res.* 251, 62–79. doi:10.1016/j.precamres.2014.06.004

Varkouhi, S., Papineau, D., and Guo, Z. (2022). Botryoidal quartz as an abiotic signature in palaeoarchean cherts of the pilbara Supergroup, western Australia. *Precambrian Res.* 383, 106876. doi:10.1016/j.precamres.2022.106876

Vuillemin, A., Ariztegui, D., De Coninck, A. S., Lücke, A., Mayr, C., Schubert, C. J., et al. (2013). Origin and significance of diagenetic concretions in sediments of Laguna Potrok Aike, southern Argentina. *J. Paleolimnol.* 50, 275–291. doi:10.1007/s10933-013-9723-9

Wei, H., Wang, X., Shi, X., Jiang, G., Tang, D., Wang, L., et al. (2019). Iodine content of the carbonates from the Doushantuo Formation and shallow ocean redox change on the ediacaran Yangtze platform, south China. *Precambrian Res.* 322, 160–169. doi:10.1016/j.precamres.2019.01.007

Xiao, S. (2004). New multicellular algal fossils and acritarchs in Doushantuo chert nodules (Neoproterozoic; Yangtze Gorges, south China). *J. Paleontol.* 78, 393–401. doi:10.1666/0022-3360(2004)078<0393:NMAFAA>2.0.CO;2

Xiao, S., Bykova, N., Kovalick, A., and Gill, B. C. (2017). Stable carbon isotopes of sedimentary kerogens and carbonaceous macrofossils from the Ediacaran Miaohe Member in South China: implications for stratigraphic correlation and sources of sedimentary organic carbon. *Precambrian Res.* 302, 171–179. doi:10.1016/j.precamres.2017.10.006

Xiao, S., Yuan, X., Steiner, M., and Knoll, A. H. (2002). Macroscopic carbonaceous compressions in a terminal Proterozoic shale: a systematic reassessment of the Miaohe Biota, South China. *South China J. Paleontol.* 76, 347–376. doi:10.1017/s0022336000041743

Ye, Q., Tong, J., An, Z., Hu, J., Tian, L., Guan, K., et al. (2019). A systematic description of new macrofossil material from the upper Ediacaran Miaohe Member in South China. *J. Syst. Palaeontol.* 17, 183–238. doi:10.1080/14772019.2017.1404499

Zaikin, A. N., and Zhabotinsky, A. M. (1970). Concentration wave propagation in two-dimensional liquid-phase self-oscillating system. *Nature* 225, 535–537. doi:10.1038/225535b0

Zhabotinsky, A. M. (1991). A history of chemical oscillations and waves. *Chaos Interdiscip. J. Nonlinear Sci.* 1, 379–386. doi:10.1063/1.165848

Zhai, X., Luo, P., Gu, Z., Jiang, H., Zhang, B., Wang, Z., et al. (2020). Microbial mineralization of botryoidal laminations in the upper ediacaran dolostones, western Yangtze platform, SW China. *J. Asian Earth Sci.* 195, 104334. doi:10.1016/j.jseaes.2020.104334

Zhou, C., Xiao, S., Wang, W., Guan, C., Ouyang, Q., and Chen, Z. (2017). The stratigraphic complexity of the middle Ediacaran carbon isotopic record in the Yangtze Gorges area, South China, and its implications for the age and chemostratigraphic significance of the Shuram excursion. *Precambrian Res.* 288, 23–38. doi:10.1016/j.precamres.2016.11.007

Zhu, M., Lu, M., Zhang, J., Zhao, F., Li, G., Yang, A., et al. (2013). Carbon isotope chemostratigraphy and sedimentary facies evolution of the Ediacaran Doushantuo Formation in western Hubei, South China. *Precambrian Res.* 225, 7–28. doi:10.1016/j.precamres.2011.07.019